AD-A270 537

THE AEROGEL MESH CONTAMINATION COLLECTOR

Steven P. Hotaling

DTIC
ELECTE
OCT. 13. 1993
S B D

**Rome Laboratory
Air Force Materiel Command
Griffiss Air Force Base, New York**

93 10 12 44

93-24061
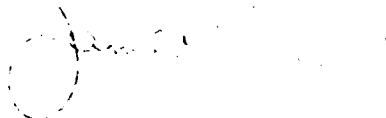
This report has been reviewed by the Rome Laboratory Public Affairs Office (PA) and is releasable to the National Technical Information Service (NTIS). At NTIS it will be releasable to the general public, including foreign nations.
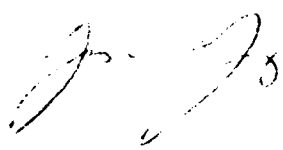
RL-TR-93-148 has been reviewed and is approved for publication.

APPROVED:

JAMES W. CUSACK, Chief
Photonics & Optics Division
Surveillance & Photonics Directorate

FOR THE COMMANDER:

JAMES W. YOUNGBERG, LtCol, USAF
Deputy Director
Surveillance & Optics Directorate

If your address has changed or if you wish to be removed from the Rome Laboratory mailing list, or if the addressee is no longer employed by your organization, please notify RL (OCPA) Griffiss AFB NY 13441-5700. This will assist us in maintaining a current mailing list.

Do not return copies of this report unless contractual obligations or notices on a specific document require that it be returned.

REPORT DOCUMENTATION PAGE

Form Approved
OMB No. 0704-0188

1. AGENCY USE ONLY (Leave Blank)	2. REPORT DATE July 1993	3. REPORT TYPE AND DATES COVERED In-House Oct 91 - Sep 92

4. TITLE AND SUBTITLE
THE AEROGEL MESH CONTAMINATION COLLECTOR

5. FUNDING NUMBERS
PE - 61101F
PR - LDFP
TA - 12
WU - K2

6. AUTHOR(S)
Steven P. Hotaling

7. PERFORMING ORGANIZATION NAME(S) AND ADDRESS(ES)
Rome Laboratory (OCPA)
25 Electronic Parkway
Griffiss AFB NY 13441-4515

8. PERFORMING ORGANIZATION REPORT NUMBER
RL-TR-93-148

9. SPONSORING/MONITORING AGENCY NAME(S) AND ADDRESS(ES)
Rome Laboratory (OCPA)
25 Electronic Parkway
Griffiss AFB NY 13441-4515

10. SPONSORING/MONITORING AGENCY REPORT NUMBER

11. SUPPLEMENTARY NOTES
Rome Laboratory Project Engineer: Steven P. Hotaling/OCPA (315) 330-3147

12a. DISTRIBUTION/AVAILABILITY STATEMENT
Approved for public release; distribution unlimited.

12b. DISTRIBUTION CODE

13. ABSTRACT (Maximum 200 words)

High performance optical and microelectronic components have ever tightening contamination specifications placed upon them. Contamination is now seen as a major reason for the degradation of space based optical systems and failure of high density integrated circuits used throughout industrial and military systems. To address this problem, contamination removal and collection techniques have been developed by Rome Laboratory (RL). However, some of these removal techniques create a flux of removed contaminants, which then may re-deposit on clean surfaces or be ejected into the environment. Current collection devices such as filters, charged metal plates or screens, and charged dielectrics have collection efficiencies and capture radii incommensurate with the new nano-scale semiconductor devices and space optics system cleanliness requirements. Presented here is a new contamination collector (patent pending). The collector (Aerogel Mesh Contamination Collector) or AMCC, collects and contains particulate and molecular contaminants either passively or used in conjunction with contamination removal devices creating a synergistic contamination control system with prevention, removal, and collection capabilities. The system is applicable to both clean room and cryogenic-vacuum conditions such as spacecraft environments.

14. SUBJECT TERMS
AMCC (Aerogel Mesh Contamination Collector), contamination collection, contamination control

15. NUMBER OF PAGES

16. PRICE CODE

17. SECURITY CLASSIFICATION OF REPORT UNCLASSIFIED	18. SECURITY CLASSIFICATION OF THIS PAGE UNCLASSIFIED	19. SECURITY CLASSIFICATION OF ABSTRACT UNCLASSIFIED	20. LIMITATION OF ABSTRACT U/L

Preface

This is the result of 9 months of research on RL project number LDFP12H2. The project was a 6.1 effort funded by AFOSR through the Office of the RL Chief Scientist , Dr. F.I. Diamond. This device, having applications to contamination control, precipitated advocacy and corporate visibility from the RL SDIO Contamination Control program managed by Capt. D.A. Dykeman. Their advocacy and support is gratefully acknowledged.

It is important to recognize the commercial applications of this and other space technology to the civilian sector. Examples of the *Dual Use* nature of the AMCC include: semiconductor processing and insitu chip package getters, cryogenic/vacuum system getters, microwave tube getters, molecular sieves and biomedical and other cleanroom filters.

i

Contents

Executive Summary

This report presents the state of the theory and practice of the Aerogel Mesh Contamination Collector (AMCC) as studied under the Rome Laboratory project LDFP 12H2. The AMCC was found to be an improvement to the prior art getter technologies, so much so that two patent applications were filed for embodiments of the AMCC.

Prototype AMCC's were fabricated in this effort, but optimization was not accomplished. This fact notwithstanding, the preliminary results showed the AMCC to be operable over a wide temperature range : $4 < T < 600$ °K. The device was found to be remarkably radiation resistant (surviving up to 100 Mrads).

The engineering tests of the AMCC suggest that the AMCC should be studied in further detail for integrated circuit and photonic modules. The AMCC is applicable to several other technology areas such as biomedical and nuclear contamination control.

BACKGROUND

Contamination control is defined as the detection, measurement, removal and collection of undesired particulate and organic species. As the design and manufacturing of optical and electronic components becomes more challenging, i.e. pristine low scatter optics and device minaturization to submicron dimensions, contamination control plays an ever increasing role. An example of the economic and technological importance of contamination control is the dominance of the Japanese in high density dynamic random access memory (DRAM) chips. Because of strict contamination control in their production processes, the Japanese were able to achieve an 11 percent higher yield than US firms [1]. This small percentage yield advantage was enough to cause the US firms to virtually drop out of this industry resulting in significant economic losses and technological dependence for the United States. Contamination also affects other industries that require ultra-pure products and processes such as biotechnology, materials research, and vacuum technology.

In 1985, the USAF Rome Laboratory (formerly RADC) identified the need for better contamination control technology to meet the stringint operational and long lifetime requirements of space optical systems. Under an initial program research and development announcement, Rome laboratory established the need to develop better contamination prevention, detection, cleaning and collection techniques. To date, most work has centered upon the detection of contamination, measurement of its effect upon optical properties, and developing insitu cleaning technologies. See the Appendix for a brief description of Contamination Phenomenology and the RL Contamination Control technologies.

Little work has been done in the importa t areas of contamination prevention and collection. If the deposition of contaminants can be prevented, cleaning will be required less often. This would impact spacecraft systems designs as decreased weight and power requirements. The impact on the semiconductor industry would be higher yeilds and reduction of costs due to waste. Contaminant collection is required to prevent the redeposition of contaminants onto the cleaned surfaces or other sensitive surfaces.

In 1991, the Rome Laboratory recognized the importance of developing contamination prevention and collection techniques and began a small in-house program to address these areas under funding from AFOSR through the office of the RL Chief Scientist. The author's ongoing research in the area of microcellular porous materials resulted in the invention of a collection device with the potential to collect and contain both particulate and molecular contaminants.

1.0 General Introduction

The presence of contamination on optical and microelectronic components degrades their operational performance and lifetimes. It is also the cause of low manufacturing yields. During the production cycle, contamination is controlled by the use of cleanrooms, process monitors, and manual cleaning techniques including solvent wipes, strippable coatings, wet-dry processes, ultrasonics and air purges. The major disadvantages of these techniques are their inability to detect and remove submicrometer particles and they tend to leave molecular residues. Some of the cleaning techniques can be damaging to delicate surfaces and/or have toxic waste products. Appendix A discusses the phenomenology of the contamination removal problem.

Once integrated into a system such as a sensor telescope, the optics are no longer accessible to monitor and manually clean. Present space satellites are currently over designed to allow for contamination induced degradation while on orbit. Over design and redundancy increases the weight of the satellite which increases the material and launch costs. Appendix A also discusses spacecraft optical contamination and contamination control as analyzed and tested in the Rome Laboratory program.

The new Aerogel Mesh Contamination Collector (AMCC), patent pending, is presented in Section 2. This device, invented at RL by Hotaling and Dykeman, is the first device to employ both active and passive means to collect and contain both particulate and molecular contaminants which is applicable across a broad spectrum of *dual use* applications.

1

The physical theory of AMCC gettering is presented in Section 3. The physical chemistry of the gas/solid interface is described in terms of the Langmuir and BET theories as applied to the AMCC's physisorption and chemisorption properties. This section considers only molecular species with treatment of particulates deferred to Section 5 and the appendix.

The AMCC engineering testing is presented in Section 4. The Thermogravimetric characteristics of the AMCC are measured using a microbalance while Fourier Transform Infrared (FT-IR) spectroscopy was performed on the offgassed species. The radiation effects are also reported in this section. Radiation effects are important because the AMCC was to be used in spacecraft applications.

To provide a complete picture of the applications of the AMCC, the appendix provides an introduction to Rome Laboratory Contamination Control techniques. These techniques are mentioned throughout the report and the appendix is intended as much for tutorial utilization as for stimulating the reader to create new applications for the AMCC.

2.0 THE AEROGEL MESH CONTAMINATION COLLECTOR (AMCC)

2.1 Introduction

The new method of contamination prevention and collection described herein employs ultra-low density silica aerogel and a highly porus aluminum mesh to capture free floating molecules and particles. Section 2.1 presents the chemical synthesis and physical chemistry of silica aerogel and the Section 2.2 presents the fabrication of the aerogel mesh contamination collector (AMCC).

The device is a heterostructure comprising a metal or ceramic foam (mesh) surrounding an ultra-low density areogel matrix. The mesh is fabricated of chemically treated metallic or ceramic foams which are chemically treated to have high mechanical strength and thermal conductivity. The aerogel completely covers the mesh structure as either an encapsulant or conformal coating. This is accomplished through the SOLGEL process [2].

RL has fabricated AMCC prototypes under this program. The AMCC operates from 4 °K to 600 °K, and in a gamma ray irradiation environment of up to 100 Mrads. Several contractors have expressed interest in the AMCC since prior art collectors have proven woefully inadequate [3].

2.2 Fabrication of The Aerogel Mesh Contamination Collector

2.2.1 Aerogel Fundamentals

The *solgel* process has been a means for producing glasses and glass ceramics for many years. The solgel process differs from conventional glass forming in that there is no melting, purifying and cooling of silica required to make the glass. Solgel is a neuvo term in the scientific parlance which indicates that the process starts out as a sol (a colloidal suspension of solid particles in a liquid) and goes through a gelation stage prior to drying. This drying process yields many possible glassy products. Figure 1 illustrates the solgel process and its products . The first step is to obtain the sol by forming a solution of solid silicate particles in a solvent (eg. tetraethylortho-silicate(TEOS) and ethanol (ETOH)). The sol is acid or base catalyzed to form a gel. A gel is a large, extended macromolecule. Figure 1 shows two paths to the gel state from the sol. The path to *xerogel* thin films (left pointing arrow) may be followed in several ways, the most common being substrate dipping and spin coating. In the dipping process, a substrate is lowered into a sol and removed with uniform velocity leaving a uniform thin film. In the spin coating process, the substrate is rotated at high angular velocity while a sol is simultaneously sprayed on it. Both of these films are later dried. The drying removes the liquid leaving a densified glassy matrix. There is considerable volumetric shrinkage during the drying/condensation stage for these xerogels, and cracking is often observed when working with large monoliths, or thin films of thicknesses greater than tens of microns.

The other path is a controlled drying state in which the sol is left at room temperature for 2-20 hours (depending upon pH concentration ratios of solvent to solute). This is the path to the right of Figure 1. If the solvent is extracted at room temperature by

controlled exposure to atmosphere, monolithic xerogels are obtained. Cracking due to stresses induced by condensation and drying are quite common for these monolithic
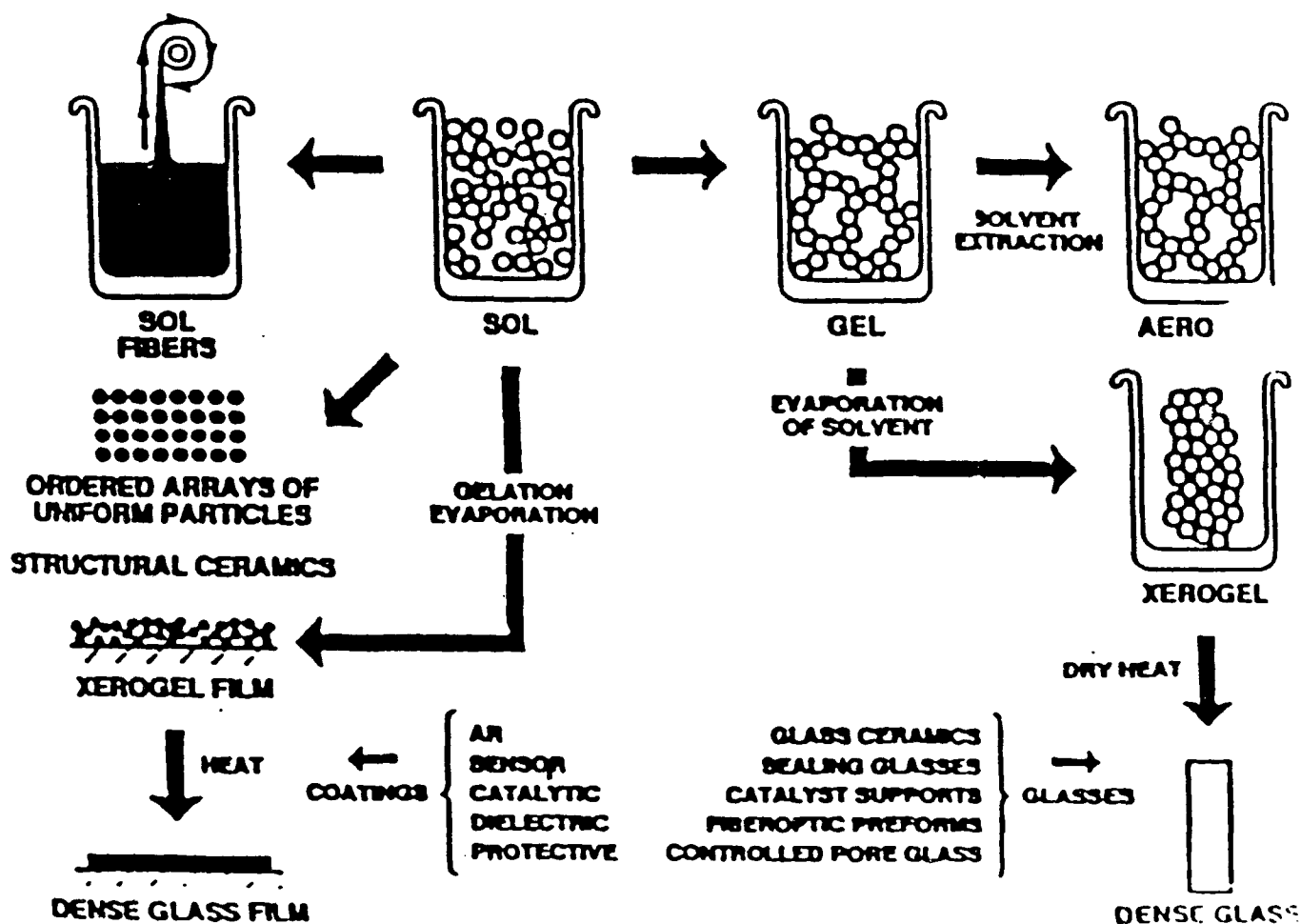

Fig. 1 Sol-Gel Processing

xerogels, which have densities of order 1 gram per cubic centimeter, and as much as a tenfold reduction in volume. The xerogel may then be sintered (at approximately 1200 C) to form a dense ceramic with density approximately that of glass (2.2 g/cm^3).

Returning to the gel state in Figure 1 and performing solvent extraction by supercritical drying under high pressures and temperatures allows the formation of an AEROGEL. The aerogel maintains its volume during solvent extraction by maintaining hydrostatic equilibrium. Thus aerogel does not exhaust its volumetric contrast; having a final density of order 0.05 to 0.6 grams per cubic centimeter. The technique of supercritical extraction to produce aerogels was developed by Kistler [4] , and has been advanced recently by Tom Tillotson and Larry Hrubish of the Lawrence Livermore National Laboratory. The Livermore technique for the production of aerogel uses ultra-pure chemical precursors and the so-called two step process in which the solvent is replaced by one with a lower critical point. This new technique uses liquid carbon dioxide to replace the alcohol or other solvents followed by supercritical extraction of CO_2. This process utilizes a critical point drying unit under much lower pressure and temperature than in the former method.

It is also possible to create fibers and membranes using solgel techniques as illustrated in Figure 1, but the current Rome Laboratory interest is in bulk aerogels and xerogel thin films (for monolithic photonic devices and lightweight optics). This report series will focus on silica aerogels almost exclusively. It is also of interest to note that non-silicate (organic) aerogels are obtainable with the solgel process and may be of future interest to Rome Laboratory.

2.2.2 Basic Aerogel Chemistry

An aerogel is a colloidal substance formed by replacing the liquid in a gel with a gas (in the most common application , air). A colloid is a solid, liquid or gaseous substance made up of very small, insoluble, nondiffusable particles that remain in suspension in a surrounding solid, liquid or gaseous medium of different matter. The dispersed phase is unaffected by gravitational forces and hence exhibits Brownian motion (as expected). Sols, aerosols (fog or smoke) and emulsions are all examples of colloids which occur in the thin film or monolithic solgel synthesis. For the most common aerogels, the precursors of colloidal preparation consist of a metal or metalloid element bounded by various ligands. The most common class of precursors used in the aerogel process are the alkoxy ligands. An alkoxy is formed by removing a proton from the hydroxyl of an alcohol as shown in equation one.

$$HO\text{-}CH_3 \implies \text{\textbullet}OCH_3 + H^+ \qquad (1)$$

A metal alkoxy is a metal organic compound which possesses an organic ligand bounded to a metal atom. Silicon tetraethoxide (also known as tetraethoxysilane or tetraethyl orthosilicate) $Si(OCH_3)_4$ is the most extensively studied metal alkoxide. Furthermore, metal alkoxides are popular precursors because they can be easily hydrolyzed:

$$Si(OR)_4 + 4H_2O \implies Si(OH)_4 + 4ROH \qquad (2)$$

$$Si(OR)_4 + H_2O \implies HO\text{-}Si(OR)_3 + ROH \qquad (3)$$

R = proton or ligand

NOTE: If R is an alkyl then •OR is an alkoxy group

7

Depending on the amount of water and catalyst present, hydrolysis may go to completion as in equation 2 or be partially hydrolyzed as indicated in equation 3. Condensation results in equations 4 and 5.

$$(OR)_3Si\text{-}OH + HO\text{-}Si(OR)_3 => (OR)_3Si\text{-}O\text{-}Si(OR)_3 + HOH \quad (4)$$

$$(OR)_3Si\text{-}OR + HO\text{-}Si(OR)_3 => (OR)_3Si\text{-}O\text{-}Si(OR)_3 + ROH \quad (5)$$
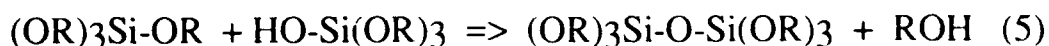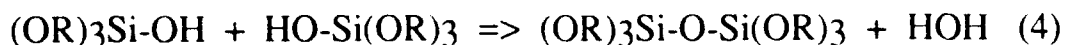
The process of condensation can soon lead to the process of polymerization of silicon containing molecules. Figure 2 depicts the formation of chains and rings by a bifunctional molecule.
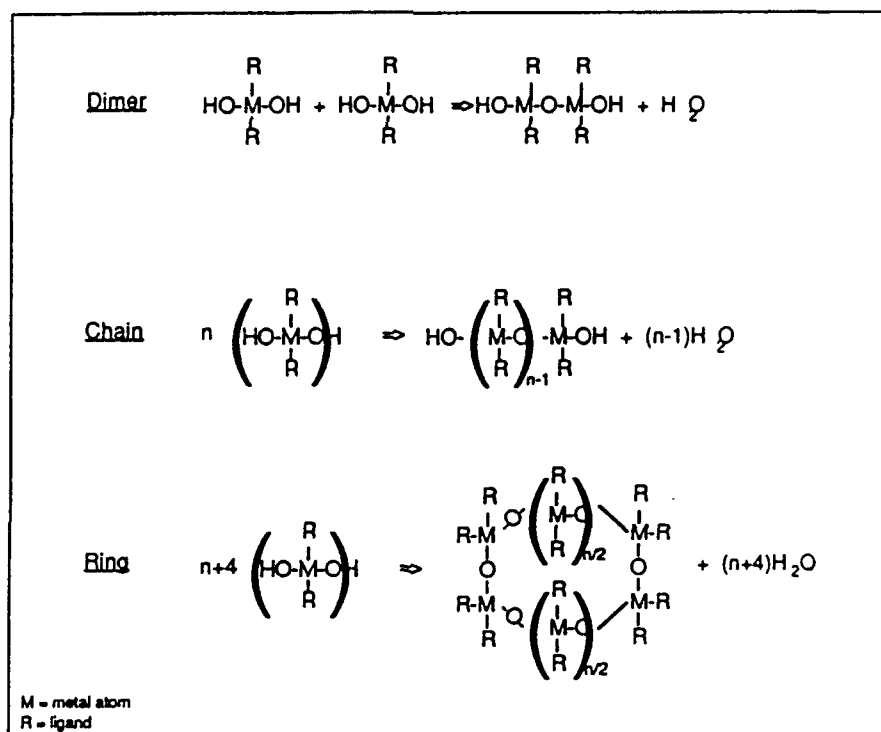

Fig. 2 Polymerization of bifunctional Monomers

As illustrated in Figures 2 and 3, the organic or metalorganic precursors can be used in the solgel process to obtain aerogels. Figure 4 illustrates the some common

8

synthesized metal alkoxides available today as they appear on the periodic table of elements. Transition metal alkoxides $M(OR)_z$, are frequently used as molecular precursors in solgel processes. Those utilized most often are titanium and zirconium. The Ti metal alkoxide is of particular interest for fabricating solgel materials with low CTE (Coefficient of Thermal Expansion). By virtue of the metal (M), the metal alkoxides are very reactive due to the OR groups being highly electronegative.

This reaction takes place in a Pyrex glass mold in the presence of a non-alcoholic basic diluent(NH_3OH). Gel time varies from 12 to 72 hours. The silica aerogel is obtained from this "alcogel" by super-critical extraction of the solvent in an autoclave. The temperature is ramped while pressure is controlled and when finished, the vessel is purged with dry nitrogen. The above molar ratios determine the reaction rates as well as the physical and chemical properties of the product.
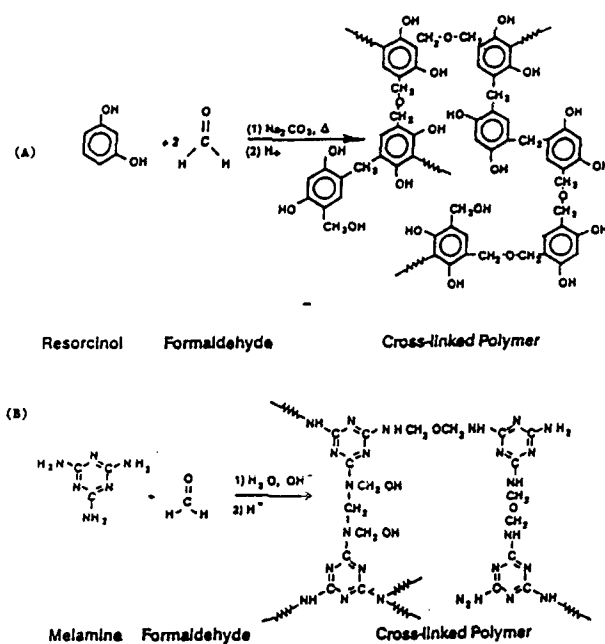

Resorcinol   Formaldehyde   Cross-linked Polymer

Melamine   Formaldehyde   Cross-linked Polymer

Fig. 3 Organic Synthesis

(A) Resorcinol and Formaldehyde Aerogel
(B) Melamine and Formaldehyde Aerogel

9

The composition of hydrophylic silica aerogels is approximately 99.6 % silicon dioxide and 0.4 % hydrogen. The density ranges from 0.003 to 0.6 g/cc. The refractive index ranges from 1.0008 to 1.126 at 632.8 nm. The porosity is 73-99.8 % . The Youngs modulus ranges between 6.9×10^4 and 3.5×10^8 Newtons per square meter. The coefficient of thermal expansion in intrinsic (undoped) material is approximately 2ppm from 293-353K. In the next paper, we will discuss the mechanical and thermal properties of ULD-Aerogels in detail.

Fig. 4 Synthesized Metal Alkoxides

2.2.2.1 Hydrolysis in Aerogel Synthesis

Hydrolysis is the reaction in which a metal ion M^{z+} reacts with HOH to form either OH- or H_3O. Such a reaction is known as a Bronsted acid-base reaction. In the Bronsted reaction H_3O and OH^- respectively, represent an acid and a base. Acid and base concentration is dependent upon the OH^-, H_3O and metal cation ion concentration. In aerogel synthesis, we are primarily concerned with H_2OM hydrolysis shown in equation below:

$$(6)$$
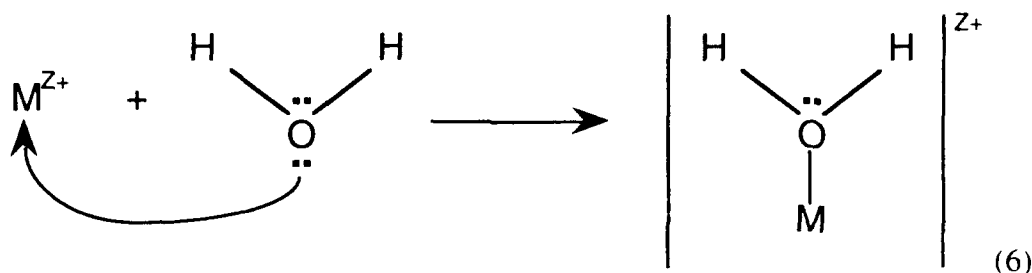
In the above diagram, the nucleophylic oxygen donates a pair of electrons from its p orbital to the d orbital of the metal cation, denoted as M^{z+}. In turn, the partial charge on the water increases thus decreasing its pH. The new polar H_2OM molecule acts as an acid - this is due to the fact that metals cations are hydrolyzed when added to an aqueous solution. Note that Group I and II metal cations do not magnanimously effect the pH of the new hydrolyzed solution. Furthermore, hydrolysis procedures may be simplified by an increased charge density placed on the water system by the metal cation. Therefore, from the charge and pH we can establish the following inorganic precursor predatory equation:

$$[M(OH_2)]^{z+} \iff [M\text{-}OH]^{(z-1)} + H^+ \iff [M=O]^{(z-2)+} + 2H^+ \qquad (7)$$

11
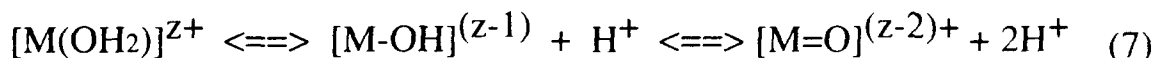
where --OHH, =O, --OH are the respective ligands aquo, oxo and hydroxo. In general any inorganic precursor may be written as:

$$[MOH_{2N-h}]^{(Z-h)+}$$
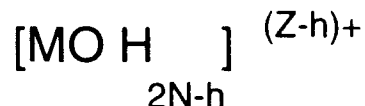
where N is coordination number of HOH molecules surrounding the metal and h is molar ratio of hydrolysis. The above equation allows us to determine the precursor. For instance, if we set h equal to zero, the precursor becomes an aquo-ion or if h equals 2N then the precursor becomes an oxy ion. If the domain is limited to $0<h<2N$ then the precursor may be any one of three complexes; oxo-hydroxo, hydroxo-aquo or hydroxo. Thus select precursors will aid the desired product in aerogel synthesis.

2.2.2.2 Condensation in Aerogel Synthesis

Condensation is the reaction that eliminates HOH molecules during the chemical bonding of monomers. Condensation occurs by either a nucleophylic substitution, better known as a SN1 reaction, or by nucleophylic addition, known as a SN2 reaction. Nucleophylic substitution may be represented by equation 8.

$$M_1\text{-}OX + M_2OY \blacktriangleright M_1\overset{\overset{\textstyle X}{\textstyle |}}{O}\text{-}M_2 + OY \tag{8}$$
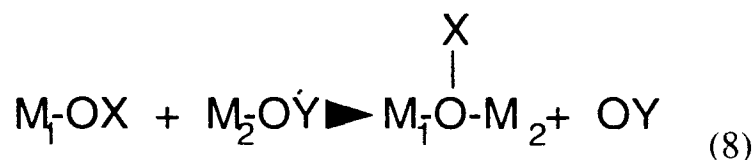
In the SN1 reaction the M2 cation bonds directly to the MOX group. The OY group then leaves. Condensation will be enhanced if the OY group is a good leaving group.

This rapidly increases condensation. The second condensation method is nucleophylic addition; equation 9.

$$\underset{1}{M}\text{-OX} + \underset{2}{M}\text{-OY} \blacktriangleright \underset{1}{M}\text{-O-}\underset{2}{\overset{\overset{\textstyle X}{\textstyle |}}{M}}\text{-OY} \tag{9}$$
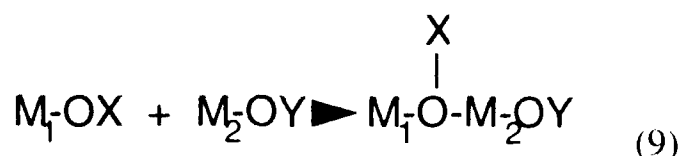
In nucleophylic addition, both polymers bond together to form a monomer. Both methods are effective, but the SN1 is preferred, since it produces a more compact and pure monomer, while the nucleophylic reaction produces a larger molecule which is more unstable than the SN1 reaction due to the presence of the OY ligand. Under certain conditions, the OY group could break away from the MOXM molecule leaving a charge on the main molecule.

Condensation occurs via two processes mechanisms: olation and oxolation. Olation is the process in which an OH group forms between two metal centers. Olation can be achieved by the abstraction of water as illustrated below in equation 10.

```
   H   H                          H   H
   O-H-O                          O-H-O
  /     \        -HOH            /     \
 M       M      =====>          M--O--M
  \     /                          H
   O-H-O
   H   H                                          (10)
```
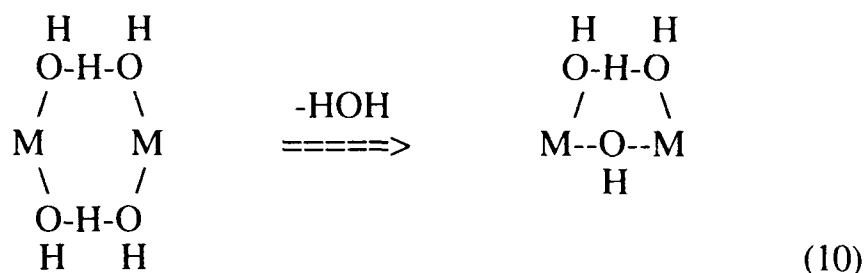
Conversely, condensation can occur by the oxolation mechanism, the reaction in which an oxo bridge is formed between two metal centers:

13

$$
\begin{array}{ccccc}
 & & & & O \\
O & & & & /\,\backslash \\
/ & + & M\text{-} & ==\!=\!> & \text{-M} \quad \text{M-} \qquad\qquad (11) \\
\text{-M} & & / & & \backslash\ / \\
 & & O & & O
\end{array}
$$
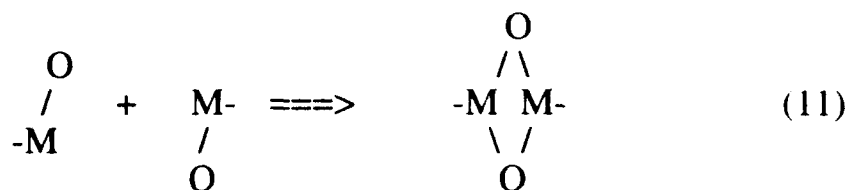
2.2.2.3 HYDROLYSIS AND CONDENSATION OF SILICATES

Silicon, one of the most abundant elements on the earth's surface, is used in the hydrolysis and condensation processes during aerogel fabrication. Tetraethoxysilane (TEOS) is the most common silicon derivative used to make polysilicate gels. The hydrolyzed TEOS goes through transesterfication to form an alkoxide of silicon. This material can be condensed to form siloxane bonds through water and/or alcohol production. This process forms a light weight fibrous silica media known as a gel. The above process can be visualized as a silica liquid that is transformed into a gel and later transformed into a solid by solvent removal. In other words, aerogel may be viewed as a dry silicon based gel (later research will involve substitution of different species to replace silicon). Different grades of aerogel may be established depending on the grade of TEOS used. The process of condensation/drying may be illustrated as shown in Figure 5 in which the formation of concave menisci signals the start of drying. Initially, the matrix is so compliant that the network adjusts itself to keep internal tension low and the radii of the menisci remain large. In the case of xerogels, the tension rises and this hydrostatic equilibrium gives way to a capillary tension in the liquid. This strengthening of the gel

14

a) Initial condition

Liquid/vapor meniscus flat

Pore liquid

Solid phase
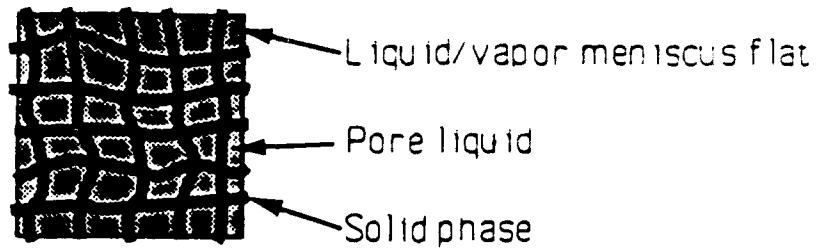
b) Constant rate period

Evaporation

Shrinkage

c) Falling rate period

Empty pores

Minimum radius of curvature
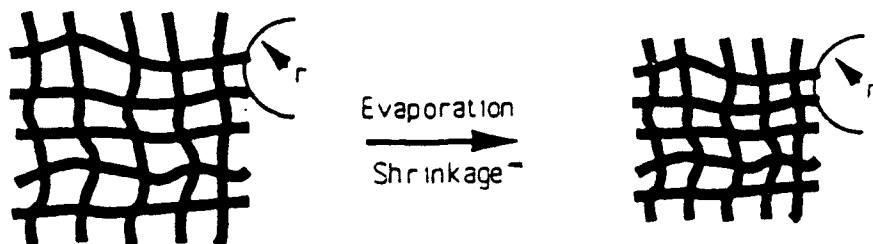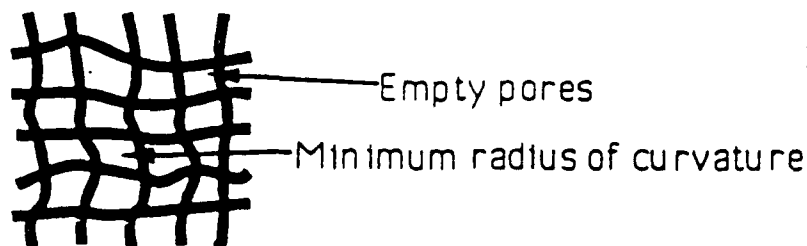
Maximum capillary pressure

$$P_R = \frac{(\gamma_{SV} - \gamma_{SL})S_p}{V_p}$$

FIG. 5 Stages of Drying

strands then gives rise to decreasing radii on the menisci. At the critical point, the radii of the menisci is equal to the average pore size and the liquid recedes into the gel leaving the glassy aerogel matrix. As previously stated for aerogel fabrication, the technique is to maintain hydrostatic equilibrium throughout the drying phase and as such, there is a lower volumetric reduction, even as the liquid is extracted at the critical point. In our process, water and alcohol removal will be accomplished with the use of a BIORAD Critical Point Dryer [20]. The RL Critical Point Dryer is shown in Figure 6.
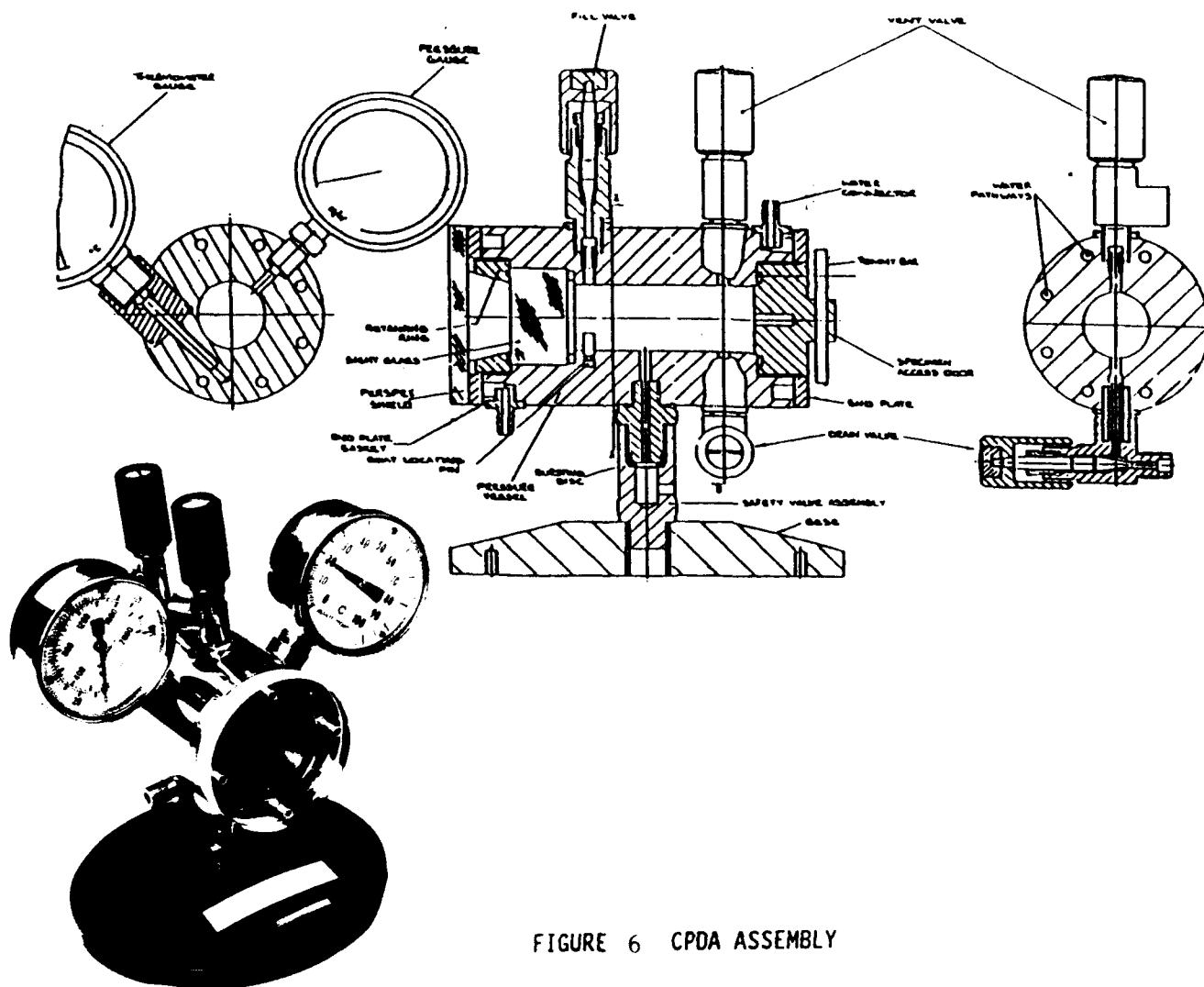
FIGURE 6   CPDA ASSEMBLY

16

2.2.2.4 AMCC Chemical Engineering/Fabrication

The fabrication of the AMCC proceeds as follows: The chemically treated mesh is placed into a mold fabricated of metal, glass or poly(propalene); depending upon the chemistry and application (details of mesh pre-treatment and mold chemistry are protected by patent laws), the sol is catalyzed, and allowed to age. The solvent is then extracted under hydrostatic equiliberium in a crytical point dryer unit or a high pressure autoclave.

A Sol is mixed with a chemical precursor (in this case Tetramethoxysilane (TMOS) and a solvent and Methanol). Tetraethoxysilane (TEOS) was also used as a precursor for these experiments. The TMOS was partially hydrolized with water in alcohol in the presence of HCL with the following molar ratios:

$$1 \text{ TMOS} : 1.3 \text{ H}_2\text{O} : 2.4 \text{ MeOH} : 10.5 \text{ HCL} \qquad (12).$$

The mixture was refluxed for 15 hours and the MeOH removed by distillation. This yields a condensed silica (cs) oil which is further hydrolized with H_2O in a 1:4 mixing ratio (1cs:4H$_2$O). This completes the hydrolysis of the precursor (TMOS). Gelation is expedited by addition of a non-alcohol catalyst (eg. NaOH). The concentration ratios of solvents and catalyst will determine the final aerogel density.

17

The mesh and SOL was placed in a critical point extraction autoclave. Without proper pre-treatment, the mesh may disintegrate upon supercritical extraction. The autoclave may be either the low-temperature or high temperature supercritical extraction processes described in section 2.2. After temperature and pressure ramps (again the details of aerogel are protected by patent laws) the suitable humidity and pore physics is obtained in the condensed aerogel. After all liquid has been removed from the system, the autoclave is purged with dry nitrogen and slowly vented. The resulting aerogel is then tested for microstructure and physical attributes.

2.3 AMCC Microstructure and Nanostructure

The ultrastructure of a sample of ULD aerogel is illustrated in Figure 6. The Figure is a photomicrograph(X64) of a sample of Silica aerogel fabricated using the high temperature high pressure supercritical extraction technique.
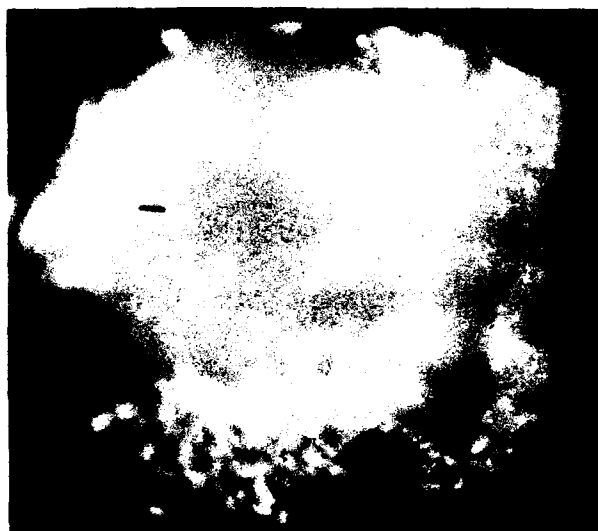
Figure 6. Photomicrograph of a sample of unpolished silica aerogel of density 340 mg/cm^3

18

This sample has a density of 349 milligrams per cubic centimeter and was cast in a mold 12 cm x 4 cm x 6 cm . This same sample of aerogel is shown in Figure 8 with a

Fig. 7 Weight Comparison: 349 mg/cc Silica Aerogel vs. Ultra Low Expansion Glass (ULE)

comparable sized monolith of ULE (Ultra Low Expansion) glass. This aerogel monolith is over 450 grams less massive than the ULE glass. This low weight will be an important savings for space based mission applications. Figure 9 shows a close-up 35mm photograph of a sample of silica aerogel of density 40 milligrams per cubic centimeter. In Figure 9, it is

interesting to note the transparency of the material which indicates potential for NLO device or transmissive optics applications. The Ultra Structure of the material appears in the

**Fig. 8   Aerogel Exhibits a Gradient in Refractive Index.
Density = 40mg/cc.**

Transmission Electron Micrographs of Figure 10. The densities of the aerogel are: 0.008 gram/cc and 0.040 gram/cc and are shown in a side by side comparison. Here, it is apparent that the ultrastructure is of differing fractal dimension for the differing density scales. This is verified by SANS (Small Angle Neutron Scattering) measurements shown in Figure 10.

$\vdash\!\!\!\!-\!\!\!\dashv$

200Å

TEM of ULD aerogel (0.008 gm/cm^3)   TEM of base/TMOS (0.04gm/cm^3)
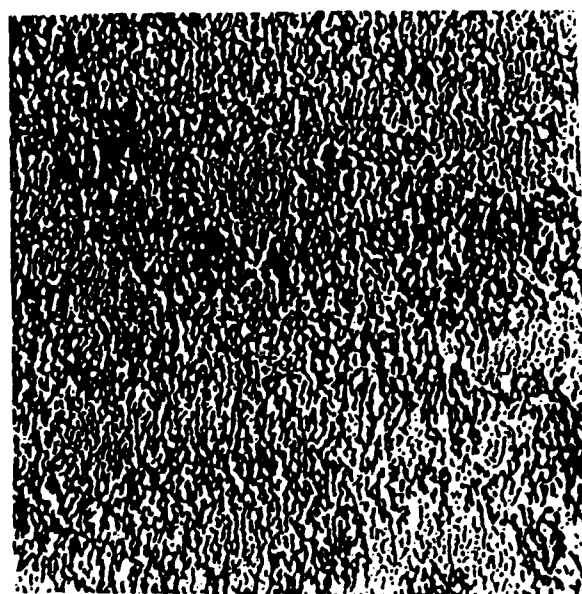
Fig. 9   Comparison of TEMs shows chain-like for ULD vs. granular for base catalysed TMOS

20

The simplest interpretation of Figures 9 and 10 is that for density ranges in the low tens of milligrams per cubic centimeter, the ultrastructure consists of polymeric chains of SiO2 m⌐'ecules connected randomly in a spatial matrix. As the density increases by an order of magnitude, this changes giving a more granular low density glassy matrix.

(A)

The ULD silica aerogels are highly transparent at visible wavelengths, compared with base catalysed TMOS aerogels that are 10 times more dense.

(B)

(C) SANS for ULD aerogel

(0.005 gm/cm³)

SANS for base cat. TMOS
aerogel (0.05 gm/cm³)
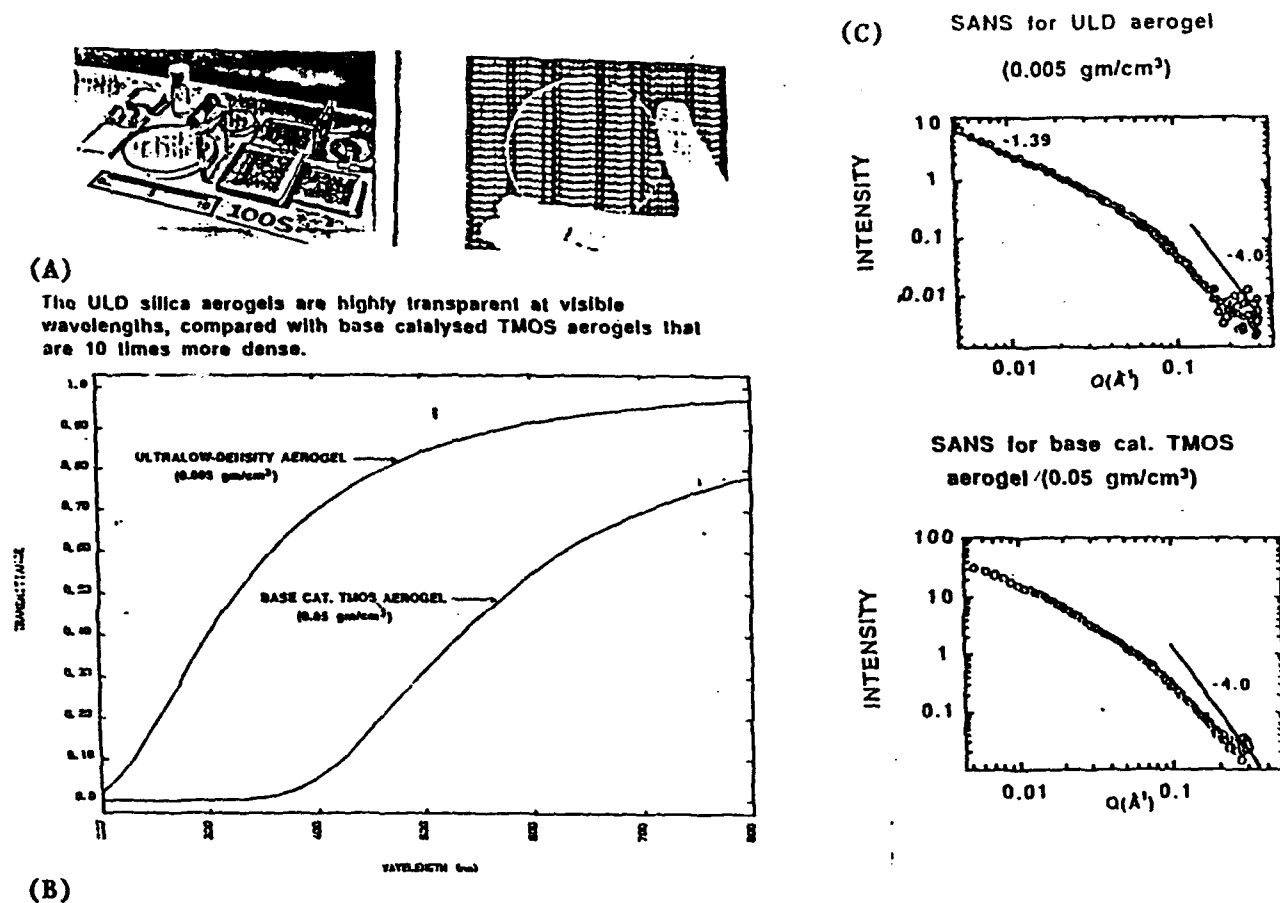
Fig. 10   Transparency, Density and Ultrastructure

A.   Various aerogel monoliths produced.
B.   Transmission spectra from UV to IR.
C.   Small angle neutron scattering results show the ultrastructure for aerogels of similiar densities as shown in B.   These data affirm the TEM results (Fig. 9) that imply that aerogels in the low tens of mg/cc density range a fractal chain linked structure whre as aerogel having densities of hundreds of mg/cc are more uniform.

3.0 AMCC Gettering

Getters [6-12] have been investigated since the turn of the century. They are materials which chemically bond to gaseous molecules. When used in vacuum systems, the result is a pumping action (sorption) which serves to maintain and/or reduce the chamber pressure. These physi-chemical adsorption, absorption, diffusion and catalysis processes are predominately surface dependent; the gas surface interface is the predominant factor in getter performance. Porous getters are materials which have large specific surface area, porosity and favorable surface/pore topology to maximize collection efficiency. Formally, we follow Wagener [6-7]:

Consider a getter which is in a vacuum system which is being supplied with a monatomic gas through a small leak valve. Further, consider the getter to be at constant temperature. The quantity of evolved gas is given by:

$$Q = \int_0^t E(t)dt \qquad (13)$$

Where : E(t) is the rate of evolution of the gas (micron-liters/s), and t is the time in seconds.

The total quantity of gas taken up by the getter is :

$$C = \int_0^t P_g G(t)dt \qquad (14)$$

Where: $P_g(t)$ is the pressure above the getter, $G(t)$ is the gettering rate (cm^3/sec).

22

In the limit as t approaches infinity, equation 14 approaches the getter capacity:

$$\lim_{t \to \infty} C \to gettercapacity \qquad (15)$$

The sorption of the getter is then given by the linear differential equation:

$$V \frac{dP}{dt} = E(t) - P_g G(t) \qquad (16)$$

Where: V is the volume of the gas

with the initial condition: $\qquad dG / dt = 0 \qquad (17)$

Integration of equation 16 subject to initial condition 17 gives:

$$P = P_0 e^{-(G/V)t} + \frac{E}{G} \sum_{1}^{\infty} (-1)^n \frac{d^n E}{dt^n} . \qquad (18)$$

If $G \geq V$, then the exponential term drops from equation 18. Further, if we assume that small perturbations in vessel pressure are negligible, then equation 18 becomes:

$$P \cong E(t) / G(t) \qquad (19).$$

23

Thus, for small perturbations in E, the pressure inside the vessel is essentially given by the ratio of the evolution and gettering rates, or that the gettering rate can be obtained from measurements of the chamber pressure, if E(t) is known.

Knudsen [25], showed that if the mean free path of the gas molecules is larger than the capillary diameter, then the flow rate through the capillary (conductance) F, depends upon the length of the capillary and the molecular weight of the gas (M) by :

$$F = \frac{66}{\sqrt{M}} \frac{d^3}{l} \times 10^3 (cm^3 / sec) \qquad (20)$$

Then, $$E = F(P_g - P_{man}) \qquad (21)$$

Where, P_{man} is the manifold pressure. Then G can be determined:

$$G = F(P_{man} - P_g) / P_g \qquad (22)$$

and if $P_{man} \rangle\rangle P_g$ then

$$G = \frac{P_{man}}{P_g} F \qquad (23)$$

The above analysis however, was valid only for a getter subjected to a monatomic gas, an isothermal experiment, and a flat surface topology over which surface coverage is defined as the areal density with no overlapping of adsorbed species. Also, the possibility of the getter evolving significant molar volumes of gas was not considered. Aerogel, as seen

24

from the photomicrographs of section 4.3.1, is a porous (open cylindrical cells) known to overlap by at least four monolayers on multicomponent gaseous species, especially if the contaminant is comprised of polar molecules [15].

This suggests that a modified Knudsen experiment can be performed as shown in Figure 11. In this experiment, designed at Rome Laboratory, the quantity of each chemical species is measured using a mass spectrom'er.
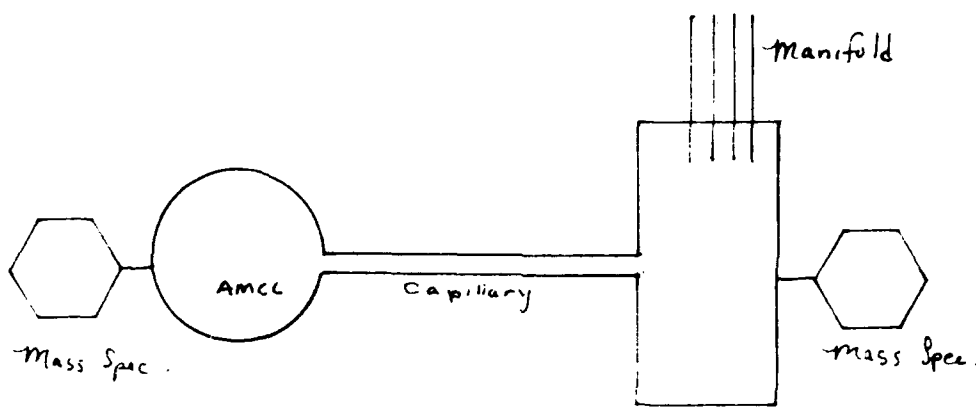
Figure 11. A Schematic of a modified Knudsen Experiment

The low density aerogels considered for the AMCC application are modeled as mass or surface fractals, in which there is little distinction between the surface and bulk. Further, the pore topology and geometry are critical in determining the physical and chemical dynamics of the *gas/solid interface*, which for practical gettering systems (as opposed to the above idealized analysis) dominates gettering.

Consider a cylindrical pore or radius of curvature r to be in contact with a contaminant vapor film of thickness th. The adsorption of gas molecules onto the surfaces of pores is attributed to capillary condensation. For capillary condensation, there is a critical pore radius and vapor film thickness for which the pore fills spontaneously irrespective of the relative pressures described in the ideal analysis above.

To allow for multilayer and Capillary Condensation, we follow the BET (Brunauer, Emmett and Teller) theory. BET is an outgrowth of Langmuir theory - the first theoretical model for the equiliberium gas adsorption process. BET has been extensively used to model adsorption in porous media, (including aerogels) for many years. It is also used as a measure of specific surface area and pore dimensions. As such, BET theory is an acceptable model for modeling the gettering dynamics of the AMCC.

As with the Knudsen theory described above, the Langmuir theory assumed that adsorption was limited to a unimolecular layer of adsorbate. The Langmuir theory will be described first as a means to describe the Knudsen-type gettering dynamics above and will also serve as an introduction to BET theory.

3.1 AMCC Adsorption using the Langmuir Theory

At equiliberium, the number of molecules adsorbed is a constant, thus the rates of adsorption and desorption are equal. The number of molecules striking a unit area of surface per unit time is:

$$\mu = \frac{p}{(2\pi m k T)^{1/2}}. \qquad (24)$$

Where p is the pressure, m is the mass of a molecule, k is Boltzmans constant and T the absolute temperature. A molecule caught in the surface potential may be modeled as shown in Figure 12 below.
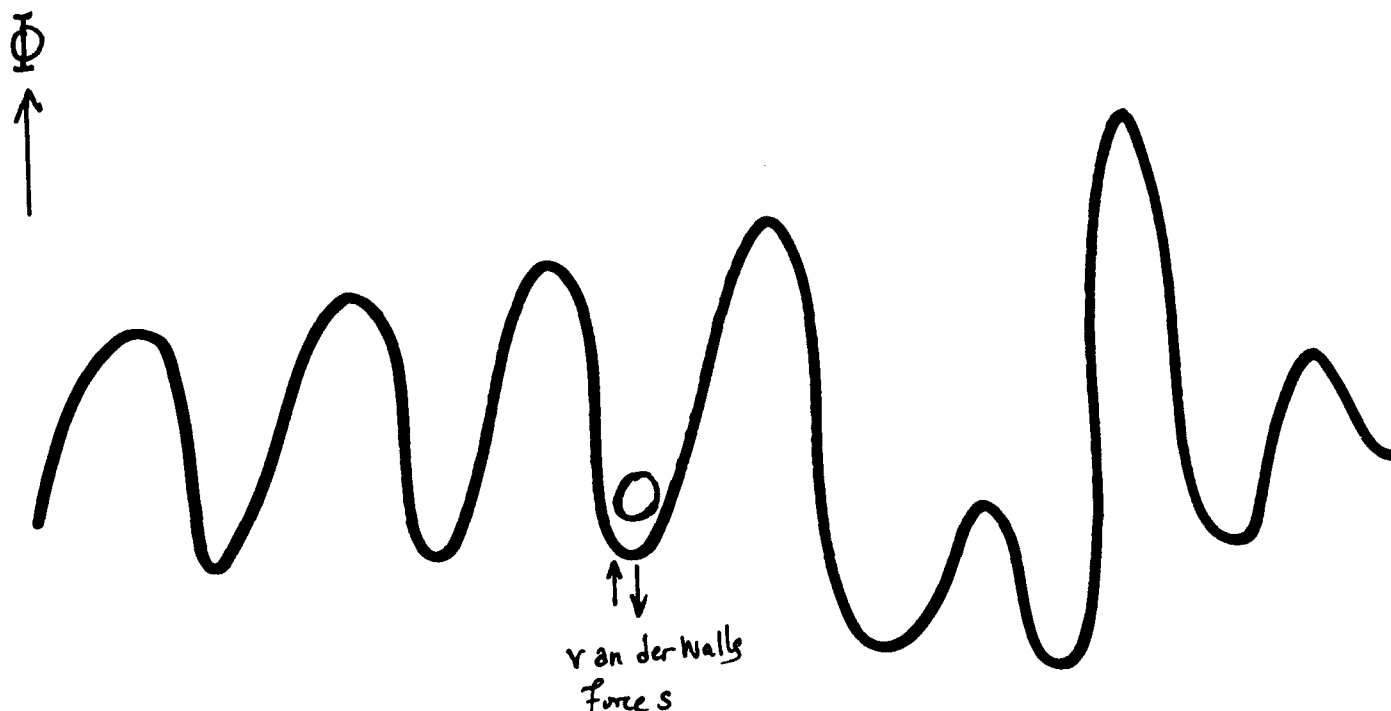
Figure 12. A cartoon of a molecule stuck in the surface potential of an adsorber.

Figures 13 and 14 below illustrate submicron and Clustered submicron

particles adsorbed onto a silicon substrate.
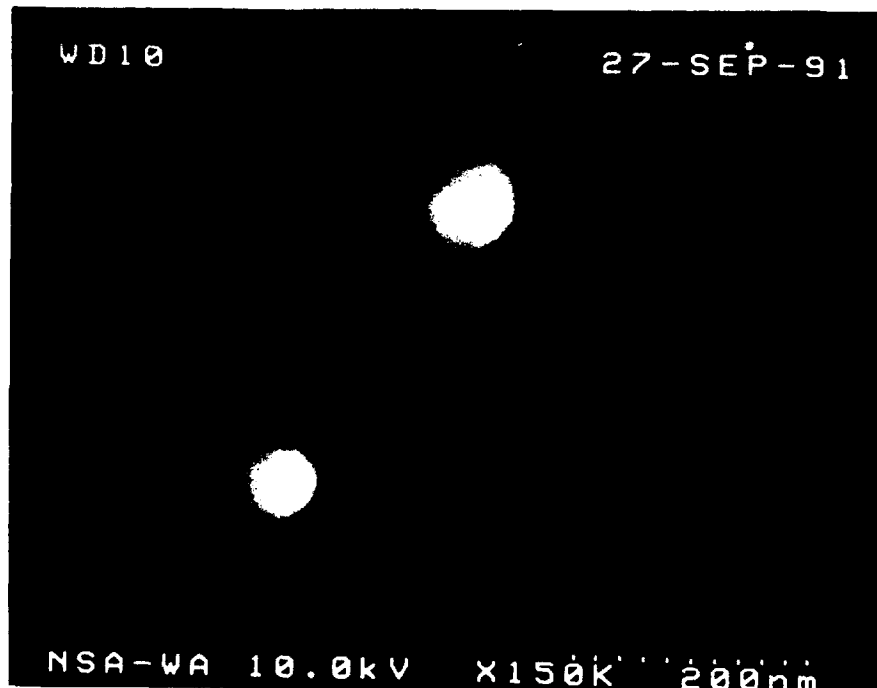
Figure 13. Field Emission Scanning Electron Micrograph (FESEM) of submicron
particles caught in the surface potential of a silicon substrate.
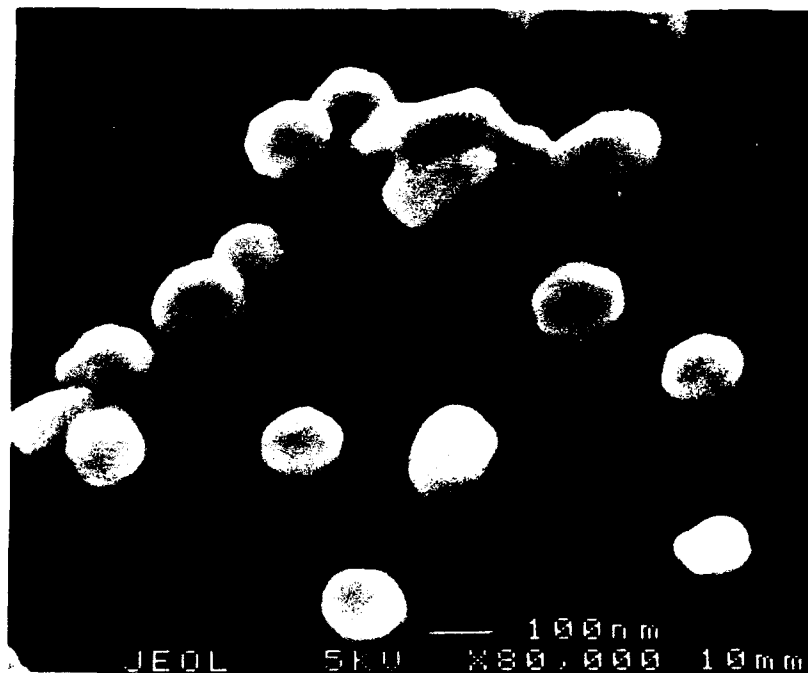
Figure 14. Clustered particles caught by the surface potential of a
Silicon wafer.

27A

Langmuir theory takes the surface potential to have very short range, hence capable of adsorbing only one molecule per surface site; molecules striking adsorbed molecules suffer elastic collisions. The rate of adsorption per unit area of surface is:

$$R_a = \mu(1 - \theta)\alpha_0 \qquad (25)$$

Where θ is the fractional surface coverage and α_0 is the condensation coefficient; the ratio of inelastic collisions to total collisions. The number of adsorbed molecules evolving from the surface per unit time is:

$$v = k_o e^{-q/kT} \qquad (26)$$

Where q is the quantity of heat evolved by adsorption, and k_o is the entropy of adsorption. The rate of desorption then is:

$$R_d = v\theta \qquad (27)$$

The above equiliberium condition then becomes:

$$\mu(1 - \theta)\alpha_0 = v\theta \qquad (28)$$

This implies that:

$$\theta = \frac{\left(\alpha_0 / v^\mu\right)}{1 + \left(\alpha_0 / v^\mu\right)} \qquad (29)$$

or that

$$\theta = \frac{bp}{1 + bp} \qquad (30)$$

Where

$$b = \frac{\alpha_0 e^{q/kT}}{k_0 (2\pi mkT)^{1/2}} \qquad (31)$$

If we assume that the surface is very sticky, then α_0 is approximately unity. If v is constant then there is constant free energy of adsorption. This agrees with the statistical and thermodynamic derivations of the Langmuir equation, and b will be constant if the free energy of adsorption is constant. The physics described by Langmuir's theory for monolayer adsorption is obtainable from statistical mechanistic derivations as well [17]:

$$b = \frac{\hbar^3}{(2\pi m)^{3/2} (kT)^{5/2}} \frac{f_a(T)}{f_g(T)} e^{q/kT} \qquad (32)$$

Where $\hbar$ is Plancks constant and $f_a(T)/f_g(T)$ is the ratio of the internal partition functions of the adsorbed and gaseous states, respectively. It is important to note that the form of the relation depends only upon the total set of states, adsorbed and gaseous thtah are accessable to the molecules at equiliberium; *not* on the mechanism of condensation or evaporation. This is irrespective of the uniformity of the surface potential energy. The important point of all this is that :

29

The Langmuir theory holds when the free energy of adsorption is constant or very nearly constant.The exponential term in b is the dominant term in the formulation; involving the heat of adsorption. For energetically heterogenous surfaces at small θ ,adsorption occurs at sites of highest energy (q is a decreasing fn of θ). Intermolecular interaction energies between physically adsorbed molecules increases the heat of adsorption, implying that the laterial interaction energy is an increasing function of θ .

These two effects compensate for each other, making q approximately constant as described above. Also, the variation in the entropy term (k_0) may compensate for the variation in enthalpy. These compensating terms cause the free energy of adsorption to be relatively constant along an adsorption isotherm. Adsorption of oxygen (curve 1) and carbon monoxide (curve 2) and carbon dioxide (curve 3) onto silica gel at zero degrees C (curves 1,2) and 100 C (curve 3), respectively is illustrated below.
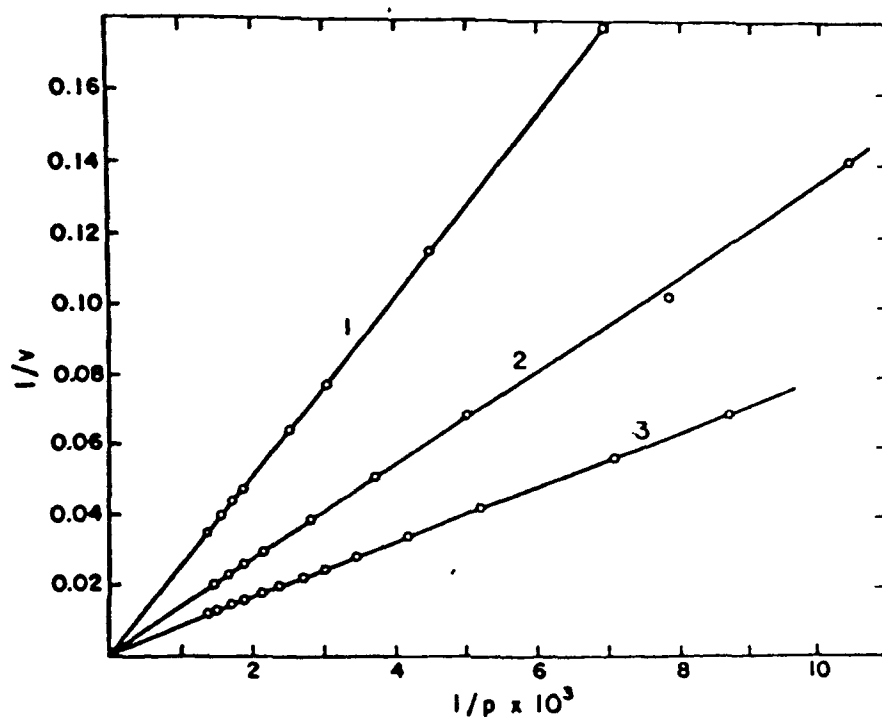
Figure 15. Linear Langmuir plots for the absorption of oxygen at 0°C (curve 1), carbon monoxide at 0°C (curve 2). and carbon dioxide at 100°C (curve 3) on silica.

30

The surface fraction, θ can be normalized as :

$$\theta = \frac{v}{v_m} \qquad (33)$$

Where v is the volume of gas adsorbed at the equiliberium pressure p and v_m is the total volume of gas required to cover the surface with gas molecules. Substiturion into the Langmuir equation gives:

$$v = \frac{v_m bp}{1 + bp} \qquad (34)$$

Which for low pressures or low adsorbate concentrations becomes: $v = v_m bp$, or that the amount of gas adsorbed becomes directly proportional to the pressure (Henry Law behavior), and for high pressures, $v=v_m$. In this latter case, saturation occurrs as a result of the pressure independence. In the intermediate region, the Langmuir equation (*) is used.

If b (recall b is related to the free energy of absorption) is constant, this equation may be put into linear form as :

$$\frac{1}{v} = \frac{1}{v_m b}\left(\frac{1}{p} + \frac{1}{v_m} \right) \qquad (35)$$

Then plotting 1/v against 1/p should present linear behavior as shown in Figure 15 above. These curves obey the Langmuir theory but not simply because they are linear, in fact, many such curves although linear, are not consistent with the theory. Linearity is a necessary but not sufficient condition for an adsorption isotherm to obey the Langmuir theory. The slope

31

and intercept of the curve yield the values of v_m and b, respectively. These must be internally consistent with each other, and further consistent with the physics of the gas/solid interface. For example, the value of v_m depends upon the surface area of the adsorbent and on the area covered by an adsorbate molecule.

This implies that v_m value obtained for the same adsorbent with differing adsorbate molecules of approximately equal size should be approximately equal. In addition, a linear adsorption isotherm with this type of internal consistency may still fail the test if the absolute value of the v_m does not agree with calculated value: given the surface area of the absorbent and size of the absorbate molecule, v_m may be calculated- and this value should agree with the value obtained from the isotherm.

3.2 AMCC Adsorption using the BET Theory

As discussed throughout this section, a theory is needed for an energetically nonuniform, porous, curved surface (aerogel) which holds over wide variations in vapor pressure and heat of adsorption. Additionally, the theory must accommodate multilayer adsorption and capillary condensation. BET theory goes a long way towards this end and will be described in this section. Although BET theory accommodates more classes of isotherms than Langmuir theory (BET includes Langmuir theory as one of its cases), There are classes of isotherms not covered by BET. These include isotherms with one or more discontinuities-some no doubt corresponding to phase changes in the absorbate.

Figure 16 illustrates the five BET absorption isotherms described by BET theory. The isotherm of Type I represents Langmuir monolayer adsorption. Type II describes non-Langmuir-type monolayer adsorption. Type III treats multilayer adsorption. Type IV and V represent mono- and multilayer adsorption with capillary condensation. The Figure is a
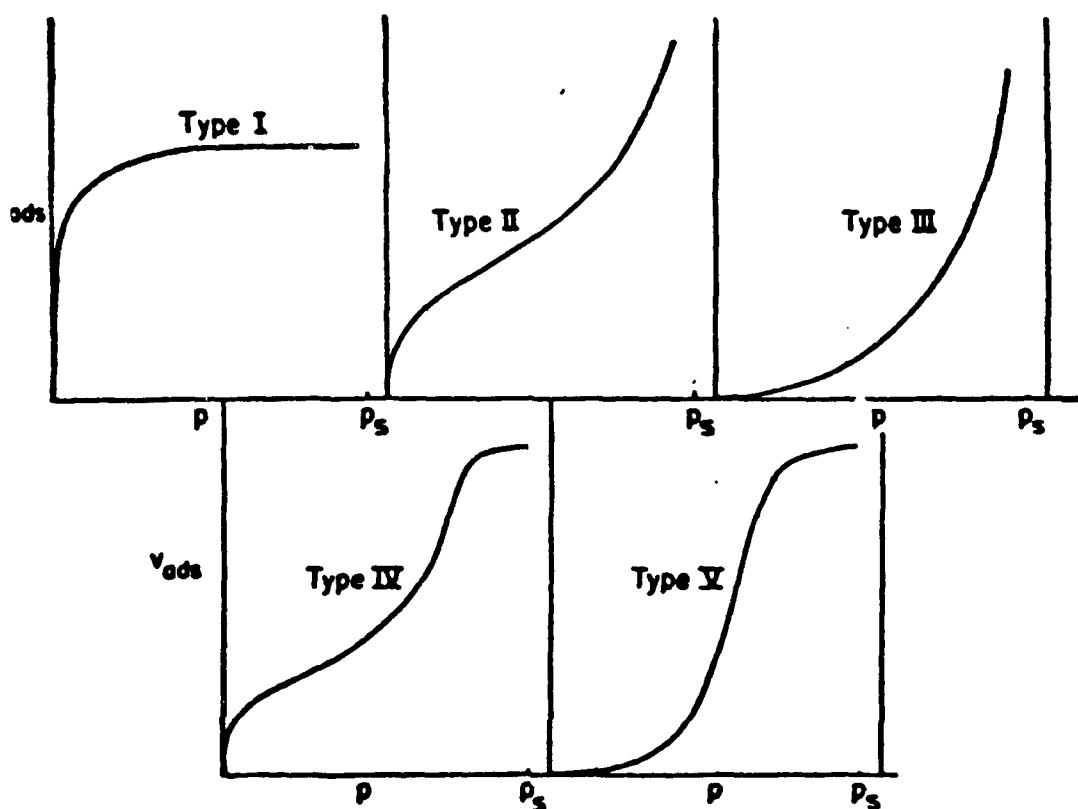
32

Figure 16. Five types of absorption isotherms considered by the BET theory. Type I: Monolayer absorption, Type II: Mono and multilayer absorption, Type III: Mono and Multilayer absorption, and Type IV and V: Monolayer, multilayer and capillary condensation.

cartoon which shows the pressure running from an arbitrarily low pressure to the saturation vapor pressure P_s.

The Type II BET theory represents multilayer absorption. If $s_0, s_1, s_2, ..., s_i, ...$ represent surfaces covered by i layers of molecules, then the equilibrium dynamics may be defined as the rate of condensation on the bare surface equals the rate of evaporation from the first layer :

$$a_1 p s_0 = b_1 s_1 e^{\left(-E_1 / RT\right)} \tag{36}$$

where p is the pressure, E_1 is the heat of absorption in the first layer, and a_1 and b_1 are constants. Since s_1 must remain constant at equilibrium, the sum of the rates of condensation and evaporation from s_1 must equal the sum of these on s_2 and so on. Equation 23 implies that

$$a_i p s_{i-1} = b_i s_i e^{\left(-E_i / RT\right)} . \tag{37}$$

Let the total surface area of the adsorbent be:

$$A = \sum_{i=0}^{i=\infty} s_i \tag{38}$$

and the total volume of adsorbate be:

$$V = v_0 \sum_{i=0}^{i=\infty} i s_i \tag{39}$$

where v_0 is the volume adsorbed on a square centimeter of surface covered by a monolayer. Then,

$$\frac{V}{A v_0} = \frac{V}{v_m} = \frac{\sum\limits_{i=0}^{i=\infty} i s_i}{\sum\limits_{i=0}^{i=\infty} s_i} \tag{40}$$

34

If we further assume that $E_i = E_L$, the heat of liquefaction of the vapor and further that $b_i/a_i = g$, (g a constant), then we have the case of assuming that the evaporation and condensation properties of molecules in the second and higher layers are liquid-like. This leads to expressing all surfaces in terms of s_0:

$$s_1 = ys_0. \tag{41}$$

where:

$$y = (a_1 / b_1) p e^{(E_1/RT)}. \tag{42}$$

Similarly s_2 may be expressed:

$$s_2 = xs_1 \tag{43}$$

where

$$x = (p / g) e^{E_L/RT}. \tag{44}$$

S_3 becomes:

$$s_3 = xs_2 = x^2 s_1 \tag{45}$$

Generally,

$$s_i = xs_{i-1} = x^{i-1} s_1 = yx^{i-1} s_0 = cx^i s_0 \tag{46}$$

$$c = y / x = (a_1 g / b_1) e^{[(E_1 - E_L)/KT]} \tag{47}$$

Substituting into equation 21 gives:

$$\frac{v}{v_m} = \frac{cs_0 \sum_{i=1}^{\infty} ix^i}{s_0 \left(1 + c \sum_{i=1}^{\infty} x^i\right)} \tag{48}$$

35

$$\frac{v}{v_m} = \frac{cs_0 \sum_{i=1}^{\infty} ix^i}{s_0\left(1 + c\sum_{i=1}^{\infty} x^i\right)} \tag{48}$$

Solutions exist for x<1. This equation becomes the BET equation:

$$\frac{V}{V_m} = \frac{cx}{(1-x)(1-c+cx)} \tag{49}$$

For free surface adsorption, an infinite number of layers may deposit. V then approaches infinity and $p=p_0$ and x=1 (obviously the above equation diverges here). Then,

$$(p_0 / g)e^{E_l/RT} = 1 \tag{50}$$

and x= p/p_0.

As with Langmuir theory, it is useful to linearize the BET equation

$$\frac{x}{v(1-x)} = \frac{1}{V_m c} + \frac{c-1}{V_m c}x \tag{51}$$

If p/p_0 is plotted against x, a straight line obtains. Several adsorption isotherms follow equation 39. If so, this allows the calculation of the specific surface area (or BET-surface area) of the adsorbing material. In fact, it was the BET measurements which first led Hotaling and Dykeman to consider applying aerogel to molecular gettering applications. The higher order BET models can be obtained from the literature[13,14,15].

Three and four parameter BET models yield the behavior for type IV and V isotherm behaviors. Although the author did not measure this behavior, it seems possible that these higher order BET models would fit AMCC adsorption data. To date, only the two parameter models have been fit; obtaining the specific surface area (Nitrogen and Helium BET areas).

4.0 AMCC Environmental Effects

4.1 AMCC Thermo-gravimetric Analysis (TGA)

From an engineering perspective, the incorporation of the AMCC into a system comprising the contamination removal technologies described in the appendix results in contamination control systems (patents pending) operable from 4 degrees Kelvin to 600 degrees Kelvin.

The engineering tests of the AMCC suggest that the AMCC should be studied in further detail for integrated circuit and photonic modules. The AMCC is applicable to several other technology areas such as biomedical and nuclear contamination control.

The AMCC prototype was tested using Thermogravimetric/Fourier Transform Infrared Spectroscopy (TGA/FT-IR). This technique combines TGA with FT-IR to obtain both the thermally induced mass loss and the identity of the evolved gaseous species by the combination of microbalance and FT-IR spectroscopy. Figure 17 is a plot of the thermal ramp and differential mass profiles of an AMCC in a TGA/FT-IR experiment. In this experiment, the temperature was increased from room temperature to 150 degrees Centigrade in three steps over a time of 18.5 minutes, in a room air atmosphere. Notice that there is no appreciable mass loss measured; fluctuations of the differential mass curve are of the order of the system detector noise level.

The FT-IR spectra from the experiment taken at various sample times are plotted on the graph of Figure 18. It is apparent that additional measurements must be taken in an inert atmosphere, since the CO_2 and H_2O backgrounds correlate with those observed in other

37

WEIGHT LOSS (PERCENT)
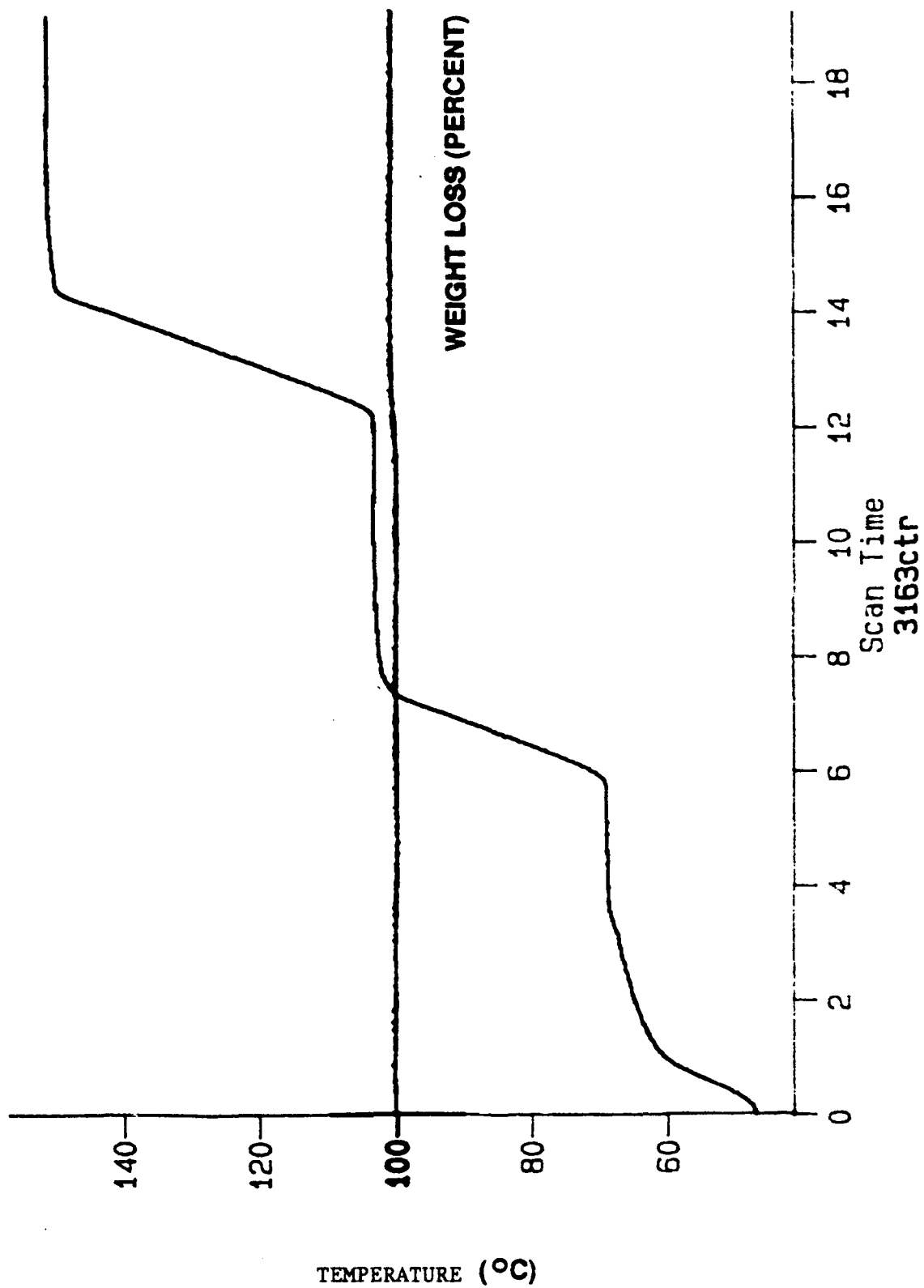
Figure 17 TGA/IR ANALYSIS OF HD001; TIME VS. TEMPERATURE

Scan Time
3163ctr

TEMPERATURE (°C)

38
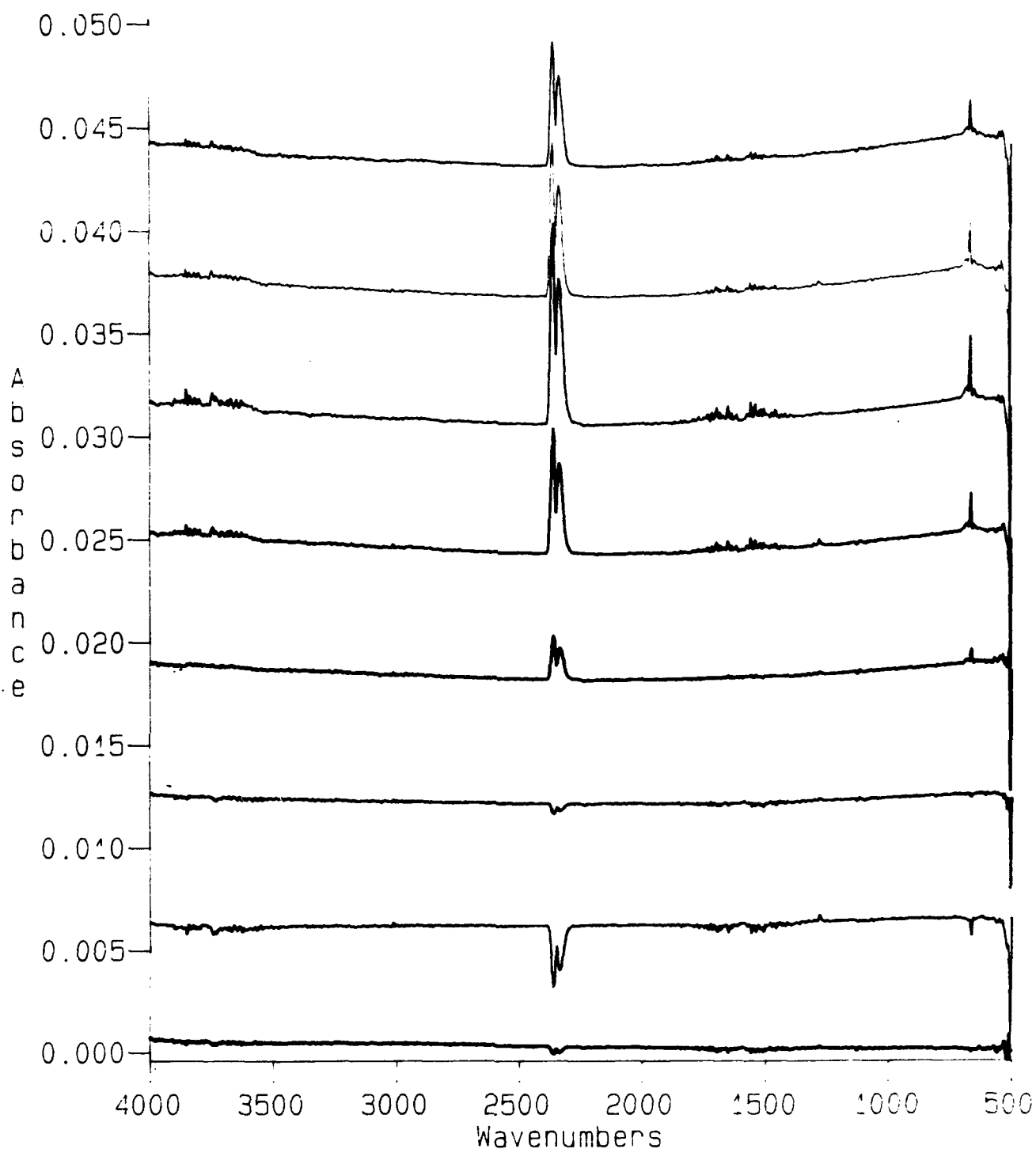
3163; Retention Time in .01min =0.31 ;
3163 (2) ; Retention Time in .01min =2.78 ;
3163 (3) ; Retention Time in .01min =4.94 ;
3163 (4) ; Retention Time in .01min =9.87 ;
3163 (5) ; Retention Time in .01min =12.65 ;
3163 (6) ; Retention Time in .01min =14.50 ;
3163 (7) ; Retention Time in .01min =16.97 ;
3163 (8) ; Retention Time in .01min =18.51 ;

Figure 18 TGA/IR ANALYSIS OF HD001; IR SPECTRA OF EVOLVED GASES
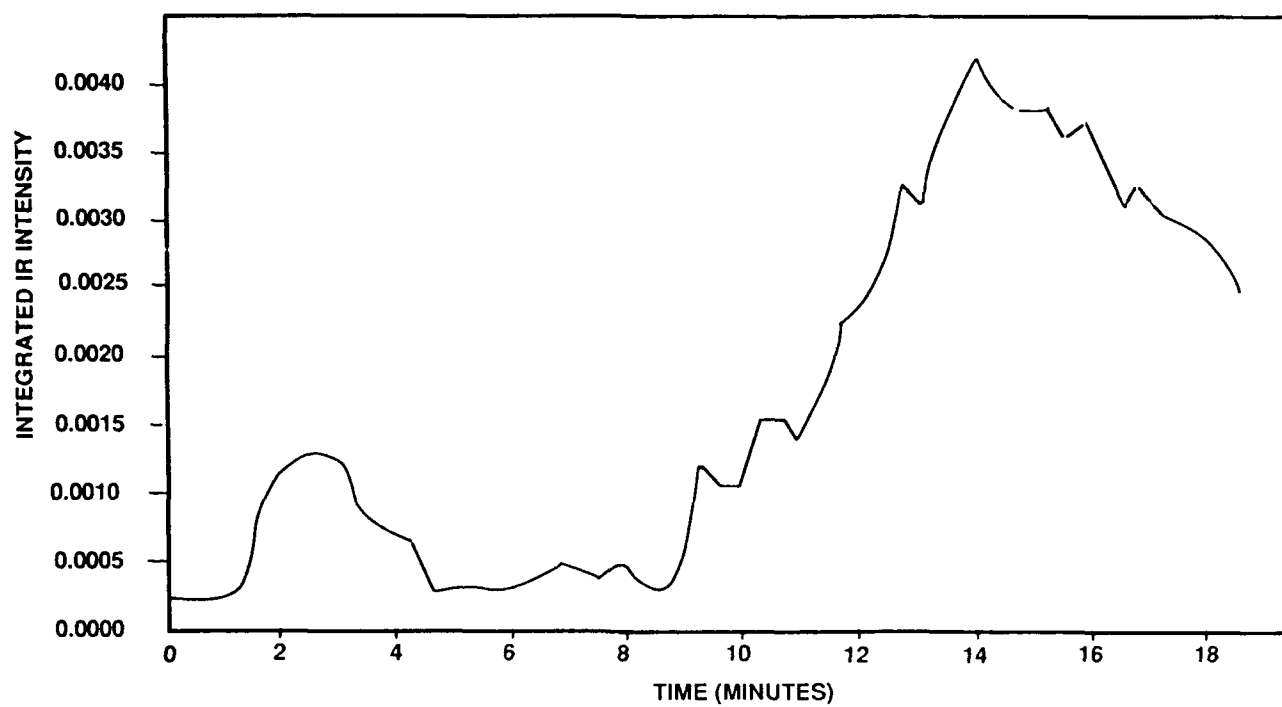
Figure 19. Integrated FT-IR Spectrum of data of Figure 18.

WEIGHT LOSS (PERCENT)

Figure 20. Thermal ramp and differential mass loss curve for 1000 C test

TEMPERATURE (°C)

room air experiments; at this time, such data is not available. The integrated IR spectral intensity curve for the data of Figure 18 is shown in Figure 19.

Figure 20 illustrates the thermal ramp and differential mass profiles of a TGA/FT-IR experiment in which the temperature was linearly ramped from room temperature to 1000 °C in a time interval of 30 minutes. Note that there is no appreciable mass loss until 210 °C, after which the differential mass loss curve shows a 3 percent mass loss. Th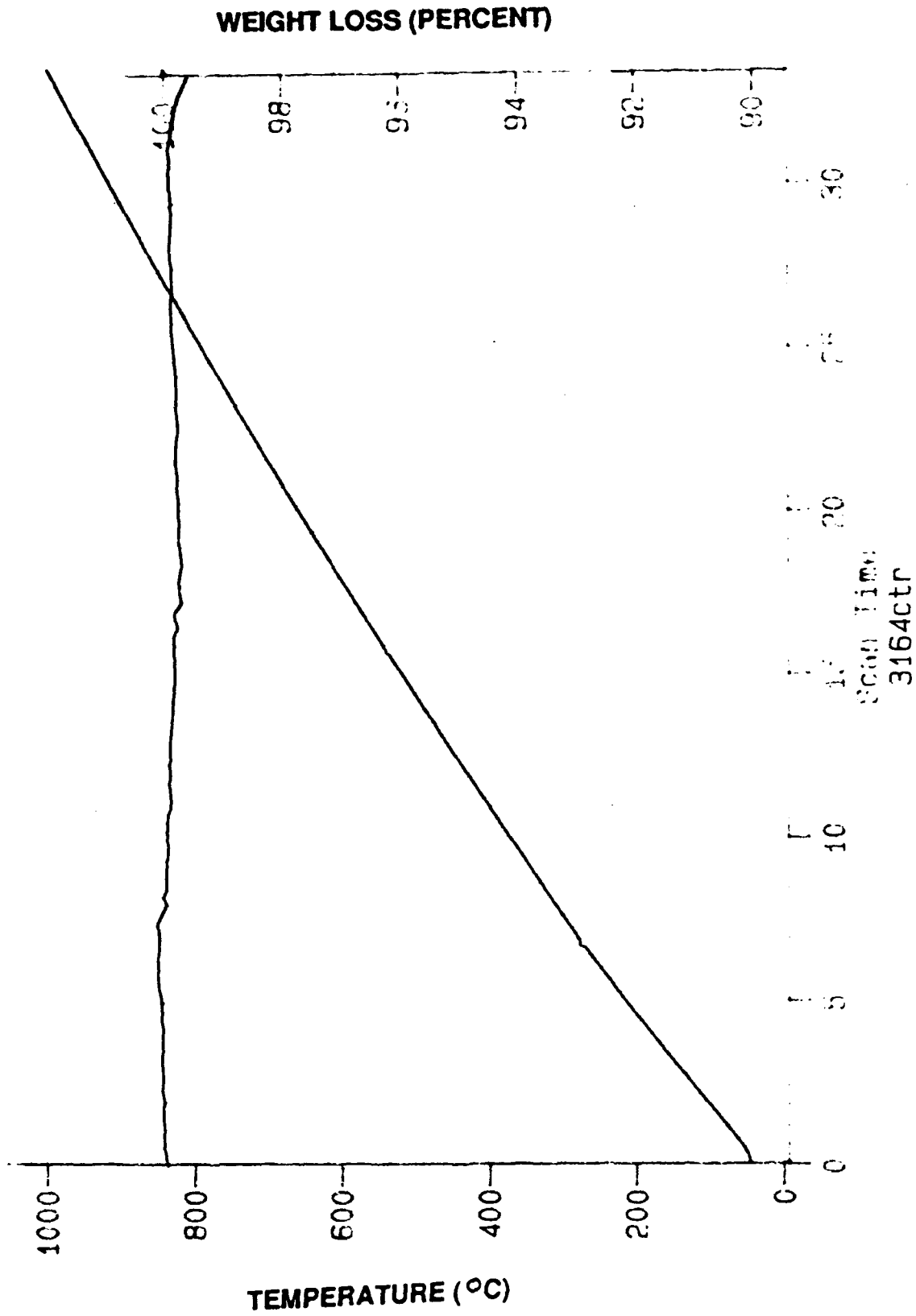e FT-IR spectra at selected temperatures is shown in Figure 21. As with the TGA/FT-IR experiment of Figure 18, there is only CO_2 and H_2O present in the desorbed gas stream. The integrated FT-IR spectrum of the evolved gas profiles of Figure 21 is shown in Figure 22. As expected, the integrated FT-IR spectrum is commensurate with the change in the TGA differential mass profile.

Preliminary AMCC offgassing rate experiments were performed using various contaminants. The experiment was performed as follows. The samples were saturated with volatile solvent molecular films in the apparatus of Figure 23. As shown in Figure 23, the solvents were heated in a boiling flask which fed vapors to the AMCC through a transfer tube into a vessel which was monitored under strong cross light. The surface color of the aerogel was used as an indicator of surface saturation. Previous work showed that the surface of aerogel turns white just prior to disintegration into silica dust (or super-saturation of the surface). The purpose of the condenser tube was to provide a controlled gas stream to enter the AMCC chamber allowing for all modes of AMCC adsorption and absorption to happen (Ref. Section 3), rather than immediate super saturation of the outer surfaces. This experiment was thus an accelerated life test of the AMCC for various contaminants. Table 4.1 gives the data obtained for these PRELIMINARY experiments (Funding was cut before complete experiments could be performed).
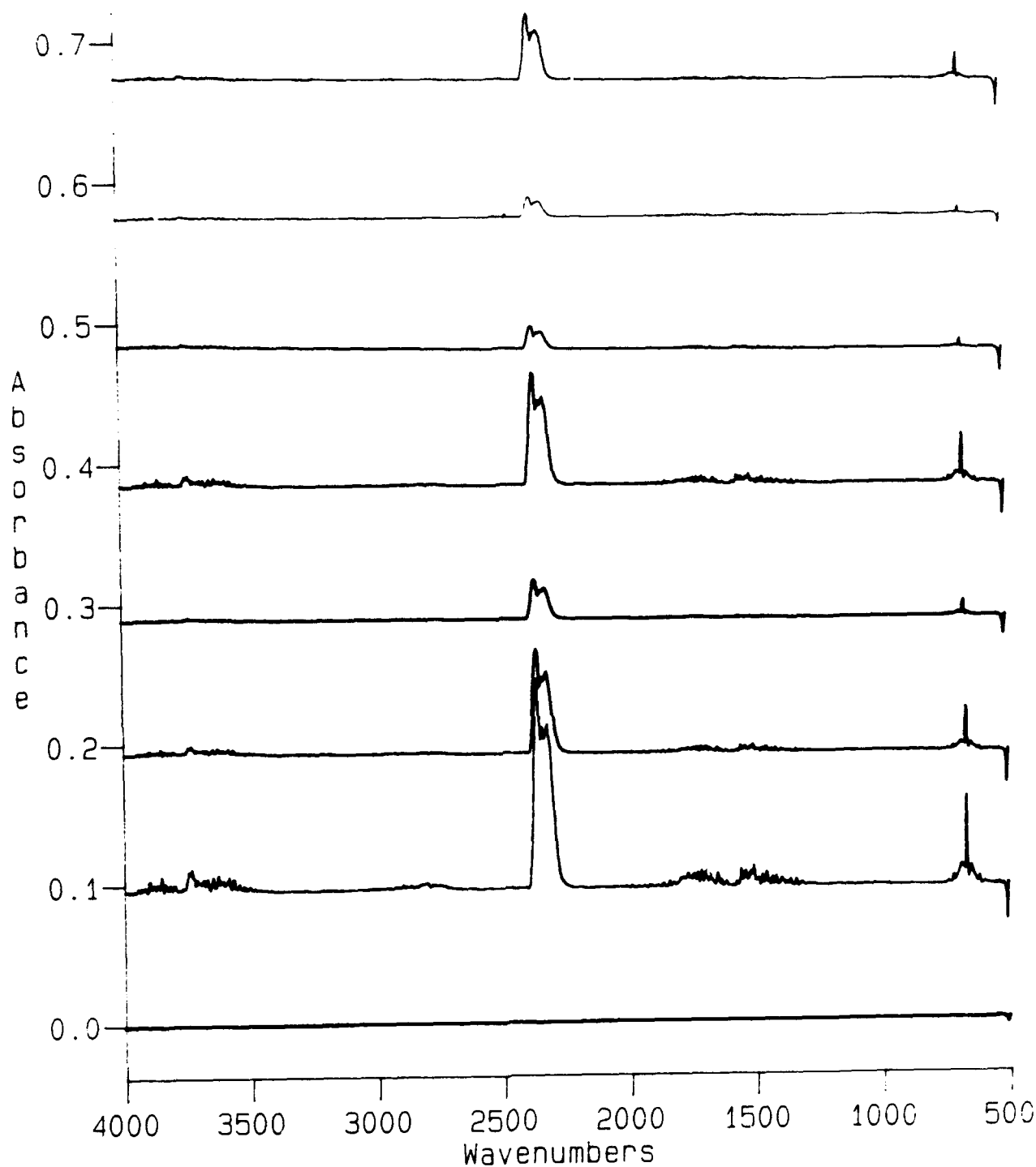
3164: Retention Time in .01min =0.62 :
3164 (2) ; Retention Time in .01min =6.79 :
3164 (3) ; Retention Time in .01min =7.71 :
3164 (4) ; Retention Time in .01min =12.03 :
3164 (5) ; Retention Time in .01min =15.73 :
3164 (6) ; Retention Time in .01min =17.28 :
3164 (7) ; Retention Time in .01min =17.89 :
3164 (8) ; Retention Time in .01min =32.70 :

Figure 21 TGA/IR ANALYSIS OF HD001; IR SPECTRA OF EVOLVED GASES

43
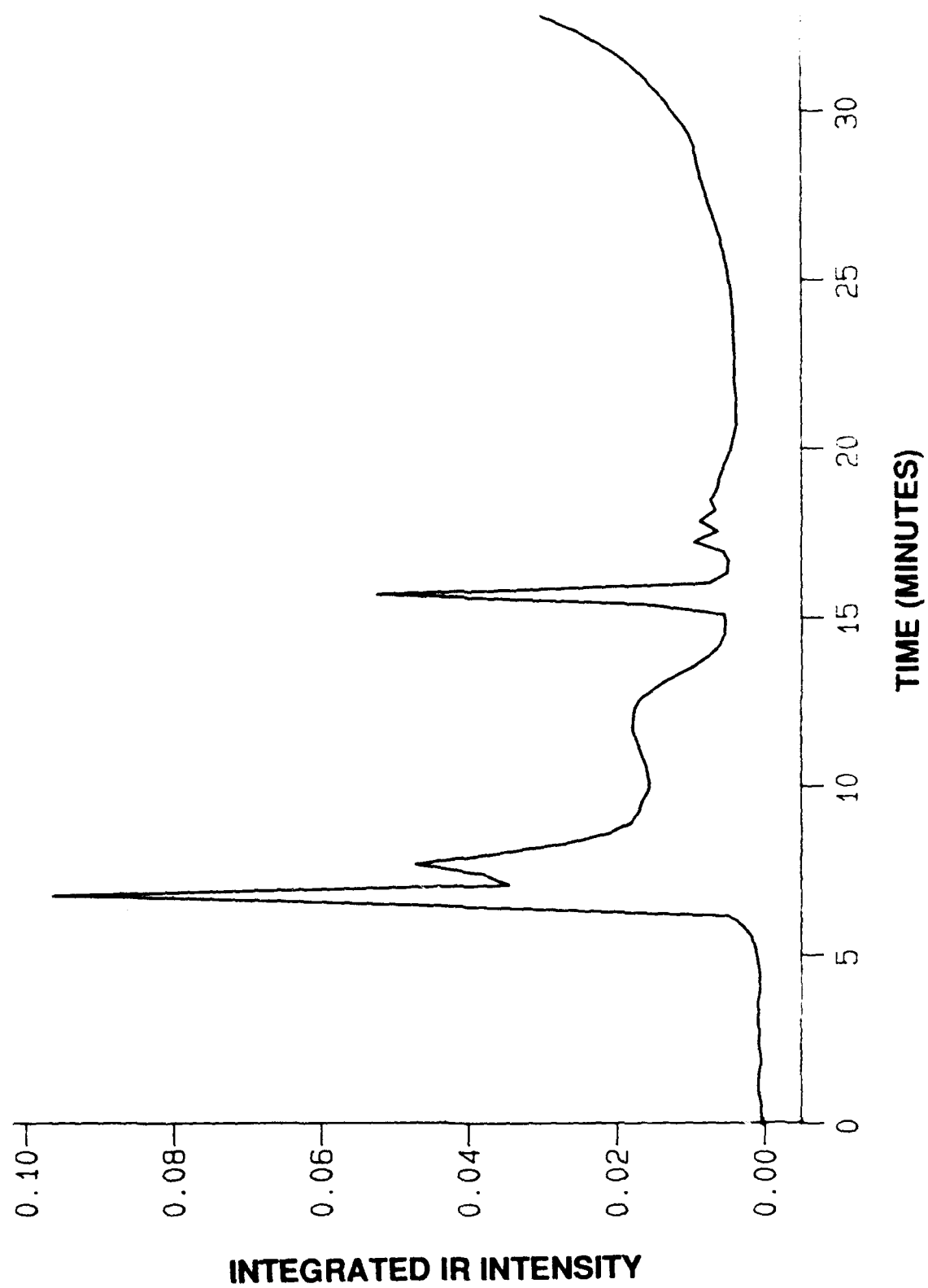
Figure 22. Integrated FT-IR spectrum corresponding to data of Figure 21.

44
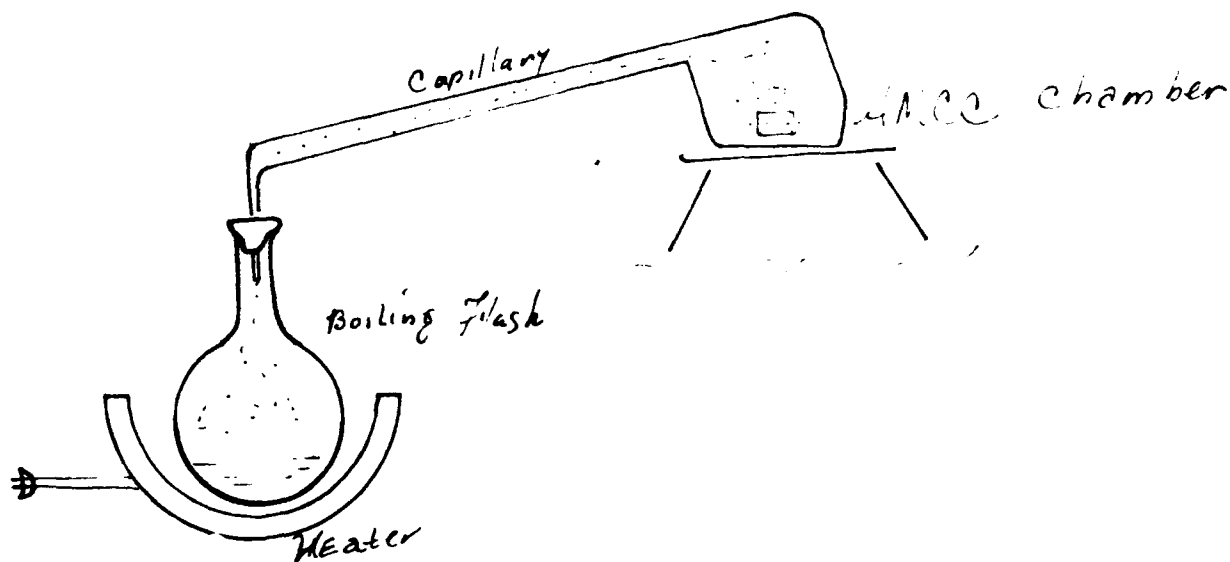
Figure 23. AMCC saturation apparatus.

Table 4.1. Preliminary AMCC Desorption Thresholds

Compound	Desorption Threshold °C
Water	210
Acetone	80
IPA	120

The importance of these experiments cannot be overstated. The current getter material used in integrated circuits just survives the military spec. temperature of 150°C. These data imply that the AMCC should be tested further for IC getters.

4.2 AMCC Radiation Effects

4.2.1 Introduction

All space optical systems must survive the radiation dose bestowed upon them by the natural space environment over their mission lifetimes. Certain military satellites have the added requirement of surviving prompt and delayed effects of high energy radiation from high altitude nuclear detonations. Although these radiation sources differ greatly in their spectral and temporal energy content, the physical mechanism of concern is the interaction of radiation with materials comprising the system. If aerogel is to be considered as a potential substrate material for space optical systems, then the effects of such radiation upon aerogel must be known. **It is quite remarkable to note that :**

The aerogel samples tested as both bulk material and reflective heterostructures showed no radiation induced metastability up to 35 Mrad γ-ray total dose. Further, there was a correlation between the Infrared transmission and the density of paramagnetic states.

The radiation may be particle-like (e.g.. α, β, p, n, e-, e+) or photonic (x-, or γ- ray) in nature. Although the energy of such high energy radiation greatly exceeds the binding energy for the electrons to nuclei in the structure, the physical reaction of these species with the absorbing medium varies distinctly. In this work for example, the pulsed electrons had very little measurable effect while x- and g- rays produced an increase in the density of localized defect states and for higher dose rates, a corresponding decrease in IR and UV/Vis transmission (color center formation). This difference being attributed to differing scattering cross sections (or penetration depths) for these species. Electrons are known to be very strongly surface absorbed as opposed to x- or g-rays, hence having lower interaction volume in the material than their photonic counterparts. This lower

46

interaction volume, considered with the low density of the aerogel is attributed to the lack of a significant electron induced radiation effect measurement. Details of the experiment appear in the next section.

In the process of traversing the sample volume, these high energy species give up their energy to absorber atoms creating defects such as: ionized atoms, free electrons, electron-positron pairs, displaced nuclei, dangling bonds, strained bonds, disclinations, dislocations, further elementary excitations of defect centers, and secondary and tertiary scattering effects. The effects of these defects upon optical elements include changes in mechanical and electro-optical properties (e.g. internal stress and strain tensors, density, Electro-optic coefficient, dielectric constant, charge separation). The mechanical changes correspond to surface deformation which destroys optical wave front integrity. Color centers decrease optical transmission, and serve as sites for space charge buildup. Changes in optical absorption correspond to increased absorption of laser radiation potentially leading to sub-optimal optical train operation. This section is a simplified review of radiation induced defect dynamics in amorphous silica and reports results of preliminary studies the author performed on the interaction of electron, x- and γ-ray radiation with (coated and uncoated) aerogel materials.

4.2.2 Absorption Physics

There are three processes responsible for photonic radiation absorption: *photoelectric absorption* ($\tau(E)$), *Compton sc' 'ering* ($\sigma(E)$), and *electron-positron pair formation.* ($\kappa(E)$). The probability of these processes occurring is expressed quantum mechanically as a scattering cross section, or absorption coefficient $\mu(E)$. This can be written as the sum of the probabilities of these processes. Here ρ is the density of the material, N is an Avagodro's number of atoms, Z is the atomic number, and A is the atomic weight. In the photoelectric process, incident photon energy (hν) is absorbed by a *bound* electron which is ejected from the atom with kinetic energy $T = h\nu - \varphi$;

where φ is the ionization potential of the electron. This electron may be adsorbed by the absorber at a defect state or ejected from the absorber. $\tau(E)$ dominates $\mu(E)$ at low energies (less than ≈ 200 KeV). $\tau(E)$ varies as Z^5 and $(hv)^{7/2}$. This dependence illustrates the fact that τ is dependent on material density and incident photon energy. As the energy increases, Compton scattering $\sigma(E)$ replaces $\tau(E)$ as the dominant term in $\mu(E)$. Here, the incident photon energy is adsorbed by the scattering atom inducing ionization, ejecting an electron and the atom radiates a photon at a lower energy. $\sigma(E)$, is proportional to Z and $(hv)^1$, since each electron scatters incident photons independently. Again, the importance of low Z materials for use in high energy environments requiring minimal radiation effects is implied. At high enough energies, both $\tau(E)$ and $\sigma(E)$ are negligible compared to $\kappa(E)$. The interaction of the incident photon with energy $hv > 2m_0c^2$ (1.02 MeV) raises an electron from a $|-\rangle$ state to a $|+\rangle$ state accordance with the Dirac Equation, creating an $e^+ - e^-$ pair. The recoil energy from the process is taken up in the Coulomb field of the nucleus. $\kappa(E)$ is proportional to Z^2, which like $\tau(E)$ increases quickly with atomic number for a given incident hv.

4.2.3 Defect Physics

Silica aerogel is an amorphous SiO_x matrix of high porosity (or a low density disordered material). The amorphous nature of the aerogel structure gives rise to a lack of translational invariance and a non-zero electronic density of bandgap states associated with localized defects. This of course differs from crystalline quartz "glass" which has the translational invariance and coordination statistics associated with a very low localized defect density (less than $10^{15} cm^{-3}$). The density of quartz, however, is a factor of six greater than that of the aerogel used herein. From absorption section above, it is clear that this density yields a higher radiation scattering cross section (or defect creation probability) for quartz than for aerogel.

As the sample is presented with a high energy radiation flux, a Si--Si bond or Si--O bond may be broken creating a defect state. There are many pathologies that may be considered possible for the resulting defect (Si dangling bond with zero to three oxygen back bonds, atomic oxygen, hydrogen dangling bonds, or Si-H). These defect centers may be neutral or charged, and thus may or may not be paramagnetic. If the centers are paramagnetic then they are detectable by standard Electron Paramagnetic Resonance (EPR). EPR measures the interaction of the magnetic moment of a paramagnetic entity (e.g. $|\uparrow\rangle$) with an externally applied magnetic field. This interaction energy is related to the cardinality of spin system, thereby allowing enumeration of the paramagnetic defect density in the sample. Even theoretically, EPR is not able to determine the *true* spin density in the system due to the existence of non-paramagnetic defect states. Charges liberated in the interaction process may further become trapped at energetically favorable defect centers changing their character to non-paramagnetic. An example of such an interaction is: $|D^0\rangle + h\nu \Rightarrow |D^+\rangle$ in which a neutral dangling bond's electronic wave function is de-localized by absorption of an incident photon's energy. The author has investigated Light induced ESR (LESR) as an electron double resonance spectroscopic technique for enumeration of non-paramagnetic defects in other disordered systems, but this was not performed in this work, which considers only paramagnetic electronic defect states (henceforth *D-center*) in aerogels. The analysis proceeds below: The spin state of the D-center is expressed by the spin Hamiltonian[9]:

$$H = \underbrace{g_0 \mu_B \vec{H}_0 \cdot \vec{S}}_{1} + \underbrace{\mu_B \vec{H}_0 \cdot \delta\tilde{g} \cdot \vec{S}}_{2} + \underbrace{\vec{I} \cdot \tilde{A} \cdot \vec{S}}_{3} + \underbrace{\vec{S}_i \cdot \tilde{D} \cdot \vec{S}_j}_{4} \qquad (52)$$

Here g_0 (=2.0023193) is the Lande-Factor of the free electron state, μ_B is the Bohr magneton

$$\mu_B = \frac{eh}{2\pi mc} = 9.274096 \times 10^{-24} \, J/T \qquad (53)$$

49

$\bar{H}_0$ is the applied magnetic field, $\bar{S}$ and $\bar{I}$ are the electron and nuclear spin operators, $\delta\tilde{g}$ is the spin orbit coupling interaction tensor, $\bar{A}$ is the hyperfine interaction tensor, and $\bar{D}$ is the spin-spin coupling interaction tensor. The first term is the Zeeman energy of a free electron with magnetic moment $(\mu_e = g_0\mu_B\bar{S})$. This term defines the external field as the direction of quantization. The defect physics manifests itself through the last three terms as perturbations. The condition for resonance is $h\nu = \langle m_s|H|m_s\rangle - \langle m_s|H|m_s - 1\rangle = g_0\mu_a H_0$, (m_s is the electron spin quantum number) which for, this case is in the microwave energy range. The second term is the same as the Zeeman term except the $\delta\tilde{g}$ tensor replaces the scalar g_0. This term expresses the g-shift observed in the radiated samples. The components of g_0 are :

$$\delta\tilde{g} = -2 \sum_{n\neq 0} \frac{\langle \delta_0|V_{so}L_i|n\rangle\langle n|L_j|\delta_0\rangle}{E_n - E_{\delta_0}} . \qquad (54)$$

Here, $|\delta_0\rangle$ is the ground state of the defect, and $|n\rangle$ is an arbitrary state, V_{so} is the potential of the spin orbit term, and $\bar{L}$ is the orbital angular momentum. The third term is the hyperfine splitting caused by the interaction of nuclear spins $\bar{I}$ with $\bar{S}$. The hyperfine interaction tensor has isotropic and anisotropic components corresponding to s-like electrons and p- or d- like electrons.

$$\tilde{A}_{iso} = (^8\!\!/_3)g_e\mu_B g_n\mu_n|\Psi(0)|^2\tilde{\delta}_{ij} \qquad (55)$$

where $\tilde{\delta}_{ij}$ is the unit tensor as would be expected for an s-like wave function. The Anisotropic components of the hyperfine tensor yield the dipole-dipole interaction for p- and d-like wave function.

$$\tilde{A}_{aniso} = g_e \mu_B g_n \mu_n \left\langle r^{-3} \right\rangle \left(\left\langle \frac{3 x_i x_j}{r^2} \right\rangle - \delta_{ij} \right)$$

(56)

The fourth term gives the spin-spin interaction term. This term is generally considered unimportant for systems with less than 10^{19} spins cm^{-3} but in high energy radiation damaged systems it is possible to introduce a topologically one- dimensional disclination type defect. This entity would have potential for spin-spin dipole interactions-- even at low overall defect densities.

4.2.4 Sample Irradiation

As described above, two populations of aerogel samples were treated with varied doses of electrons, x- and γ-rays. The first sample type was bulk unpolished silica aerogel of density 347 mg/cm^3. These samples were cut into bars with square cross section (0.6 cm x 0.6 cm $\pm$ .5 mm) for calibrated transmission and absorption measurement within the sample family. The second family of samples of aerogel consisted of polished, SiO_2-planarized aerogel (density = 450 mg/cm^3) coated with a reflective aluminum thin film. Table 4.2 gives the details of the sample population characteristics and irradiation treatment.

As displayed in Table 4.2, the experimental measures of radiation effects upon the bulk aerogel samples were EPR and transmission mode Fourier Transform-Infrared (FT-IR) and UV/Vis spectrophotometry. For the coated samples, FT-IR reflection mode spectrophotometry was used.

TABLE 4.2

INCIDENT RADIATION	SAMPLE TYPE	
	I. BULK	II. MIRROR
Electrons[1]	14.33 Krad	------------
X-ray[1]	20.0 rad	------------
γ-ray[2]	0-100 Mrad	0-100 Mrad

1: Electron Source: Linear Accelearator at Rome Laboratory (Hanscom AFB) dose rate : 2.17×10^{10} rad/sec. X-rays generated by focusing LINAC beam on a Bremsstrahlung target. X-ray dose rate: 1.56×10^{8} rad/sec. Total dose measured by PIN diode and TLD techniques.

2: Gamma Ray Source: ^{60}CO with dose rate of 2 Mrad/hr. Total dose measured by callorimeter.

Figure 24 shows the UV/Vis transmission spectra for the bulk aerogel samples subjected to 10 Mrad of gamma ray irradiation. The dose rate was 2 Mrad/hour with a temperature of approximately 80 C at the samples. There was no visible evidence of aerogel photo darkening while the co-treated Corning 7059 glass slide appeared brown in color. The visible spectra showed no change in transmittance, as illustrated in the Figure.
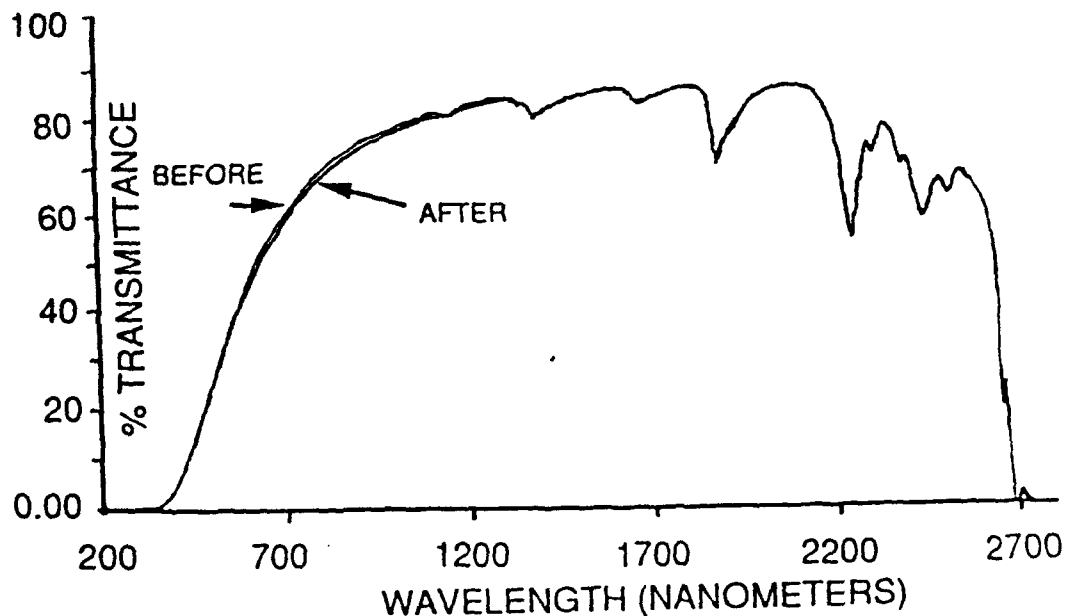
Figure 24 UV/VIS Transmission Spectra for a sample of aerogel before and After irradiation with 10 Mrads Gamma Radiation

The IR transmission likewise showed no notable change. The IR reflection spectra for the coated aerogel samples are shown in Figure 25 (R refers to radiated sample). These curves are essentially flat across wavelengths from two to five microns, except for the presence of H_2O and CO_2 absorption bands. These samples received 35 Mrad of gamma radiation.
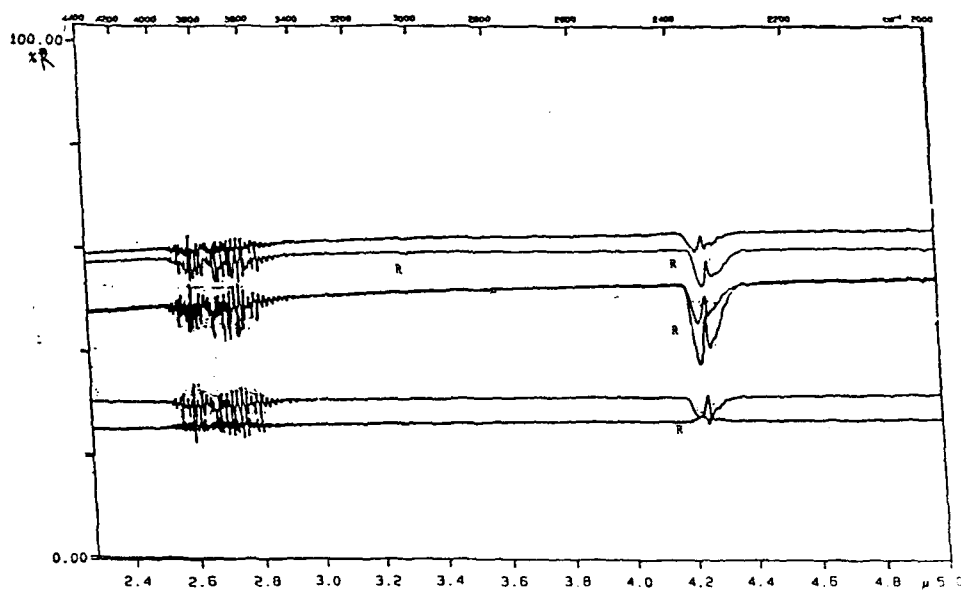

Figure 25. FT-IR Spectra of three samples of aerogel after treatment with 10 Mrads Gamma Radiation

53

Figure 26 is a plot of the EPR-measured defect density (Si dangling bond signature) for samples of bulk aerogel irradiated to a total x-ray dose of 100 Mrad (circles) and cooresponding
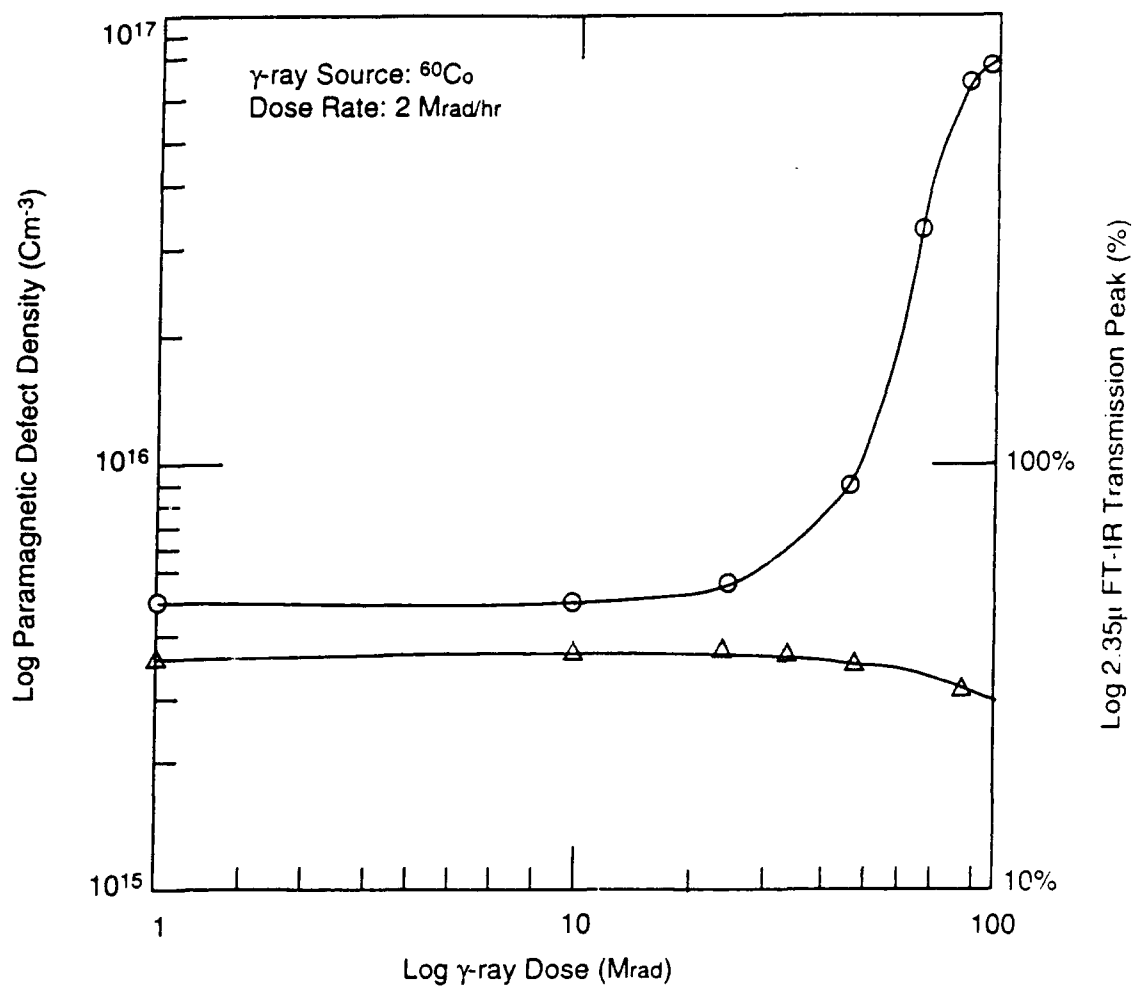

Figure 26. The paramagmetic defect density (circles) and the IR transmission of the .2.35 micron transmission peak (triangles) plotted versus gamma ray dose.

2.35 micron FT-IR transmission peak height for these data. It is remarkable that there is negligible increase in spin density *and* no decrease in IR transmission till 35 Mrad. It is even more interesting to note the exponential correlation between these data as plotted in Figure 27. By
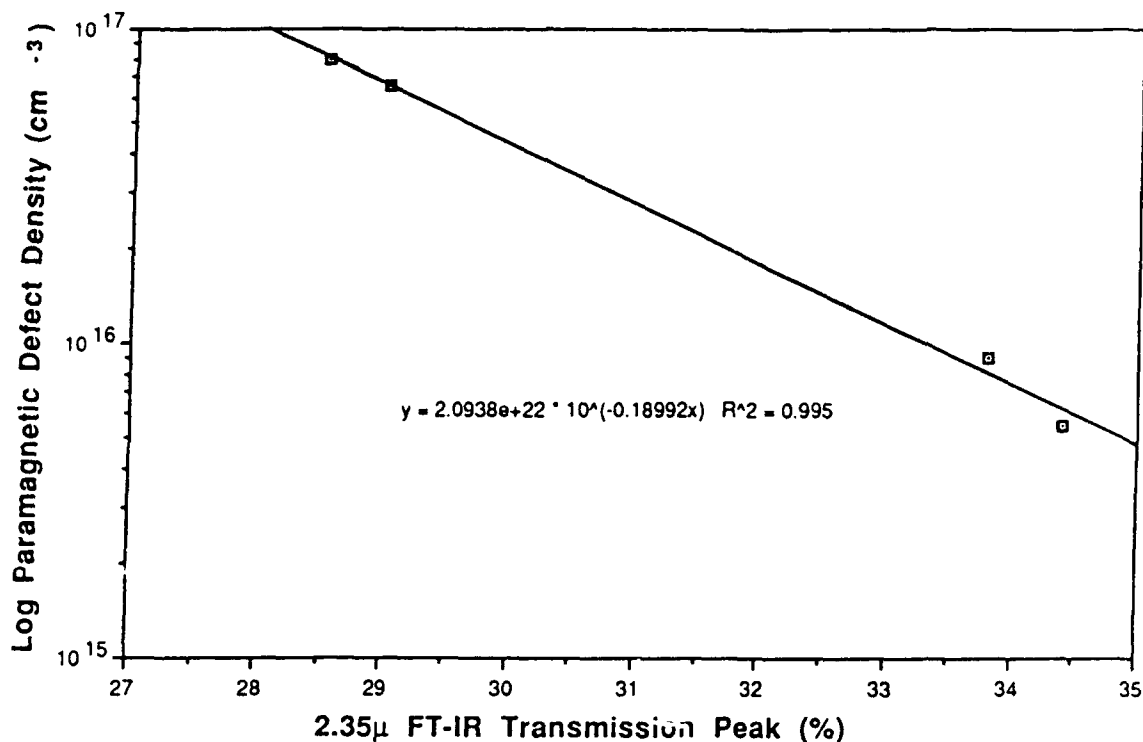

Figure 27 The exponential relation between paramagnetic defect density and the 2.35 micron FT-IR transmission peak.

increasing the receiver gain, the magnetic field scan range and magnetic field modulation amplitude while being careful not to be in nonlinear operating regimes (power saturation and modulation amplitude cutoff), the presence of anisotropic hyperfine satellites appeared in the samples treated with 80, 90 and 100 Mrad of gamma radiation. The cleanest signature (100 Mrad case) is illustrated in Figure 28.
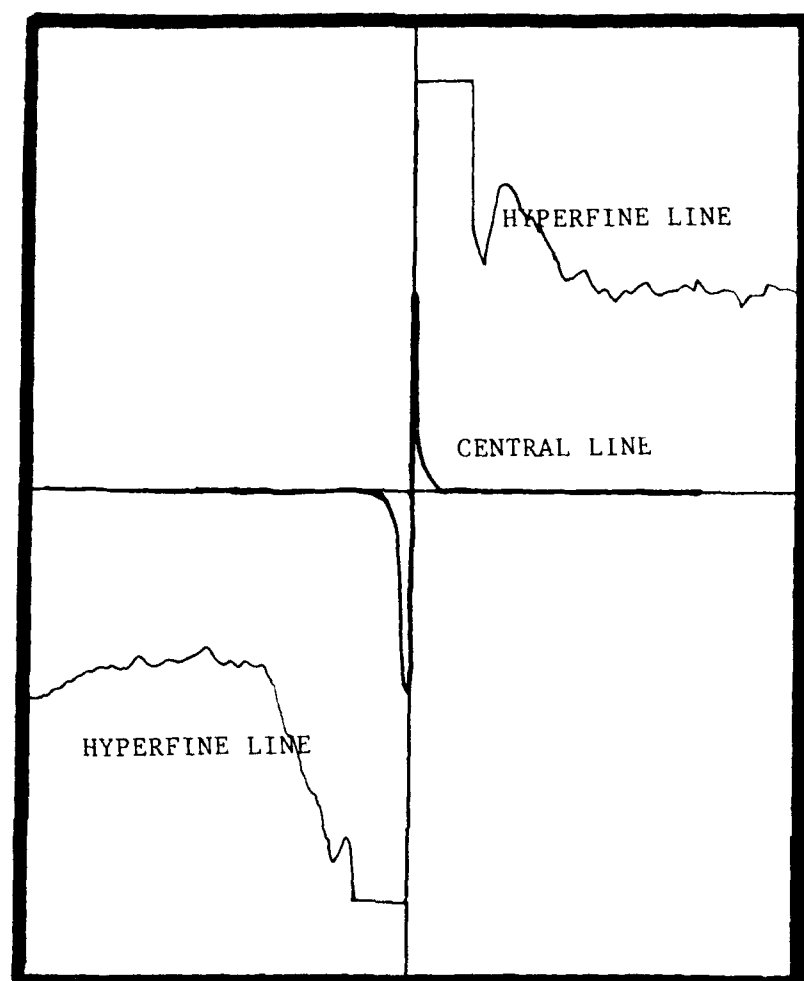
Figure 28. The EPR Hyperfine satellites from bulk aerogel sample after 100 mrad gamma irradiation. The anisotropic nature of these satellites is interesting, and suggests further work.

## 5.0 AMCC/Jet Spray Contamination Control System (Patent Pending)

Prior art for these "getters" (devices which perform contaminant capture have been called getters since the early days of vacuum science) includes metal mesh, charged plates (kilovolt charge) and charged dielectric plates. However, these systems have several problems [17]. The metal mesh (see Figure 29) suffers from being brittle and having higher desorption rates and ablation probabilities than are acceptable. The charged plates require kilovolts of potential which is unacceptable on a satellite, due to a high probability of arcing in the space environment. Charged dielectrics have capture radii far too low to be useful in practice (approx. a centimeter). Figure 30 illustrates the poor performance of the charged plates and dielectrics.

Our new design is a significant improvement, achievable through the combination of the physical and chemical properties of the aerogel and metalic mesh. The aerogel used is partially hydrophylic, organophilic, porus, posesses high BET surface area, and has a high compliance tensor in low temperature enviroments. The aerogel may be chemically doped to yield some degree of thermal conductivity which allows for bulk diffusion of surface adsorbed species. The pores (cylindrical geometry) have dimensions ranging from nanometers to microns, depending upon density, and differing density gels may be combined in the same heterostructure. The physical properties of the metal mesh are structural strength, high thermal conductivity, and the ability to attach mounting fixtures.

The mesh hence serves as the skeletal gridwork supporting the aerogel in space as well as a thermal source or sink. The symbiotic relationship between the properties of the two AMCC constituents is the way in which the materials work together in the case of a hypervelocity particle impact scenerio, such as in a cryogenic spacecraft application (see micrometeroite crater of Figure 3). In the event of such an impact, the aerogel, if unsupported could fracture. The metal mesh samples tested have shown similiar behavior
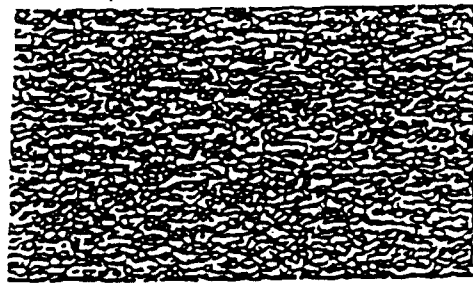
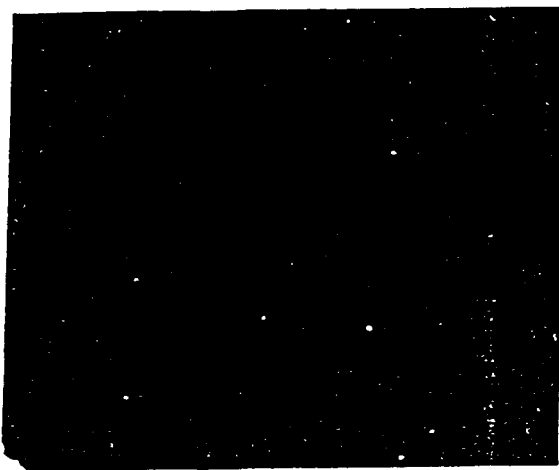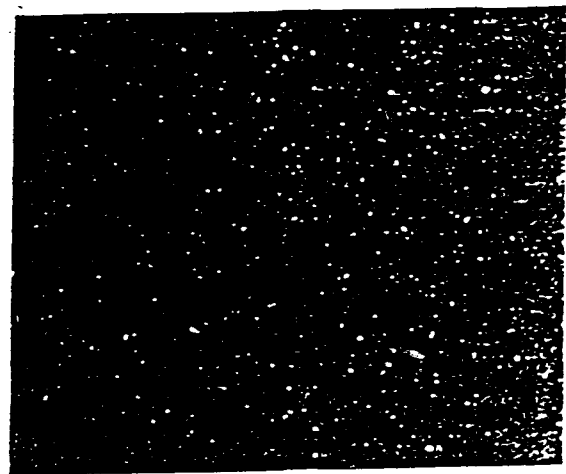20 pores
per inch
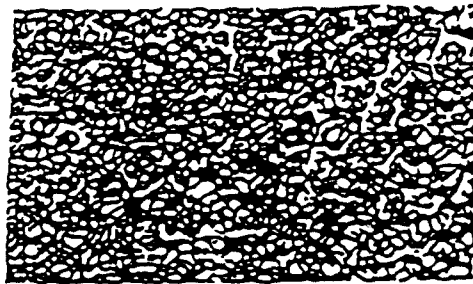
10 pores
per inch

Figure 29.   Metal mesh with different porosities

Charged Dielectric

Anti-Static Material

Figure 30.   The anti-static material is a better collector of particles than the
charged dielectric.

59

with the result of creating secondary contaminants for the system. This effect is obviated by the AMCC in that, the thick aerogel covering on the metal mesh ligaments will slow the incoming projectile and absorb some of the impact, thus decreasing the probability of mesh ligament ablation. In the event of ablation, the thickness of the AMCC heterostructure serves to collect and contain secondary and higher order debris.

Thus, the synergism of the physical and chemical properties of the aerogel and metal mesh yield a getter which may be used as:

a. an active getter which may be alternatively cooled and heated to attract moleculars and physisorb them onto the gel surface, and allow for diffusion into the bulk of the material,

b. a passive getter which may be viewed as a large area sticky surface (flypaper) which collects and contains both moleculars and particulate contaminants.

Molecular collection by the aerogel surface is illustrated in Figures 31 and 33. Figure 31 is an optical micrograph taken at a magnification of 65x of a water vapor film on aerogel of density 83 miligrams per cubic centimeter (mg/cc). Note the discoloration of the aerogel in the region of absorption. This collection was performed under ambient conditions. Microscopic analysis showed that not only was physical adsorption at the surface evident, but also that the water molecules had diffused microns into the bulk aerogel material. Figure 32 is a SEM micrograph of the surface of an aerogel sample cut from the

Figure 31. A sample of 83 mg/cc aerogel with a molecular film absorbed onto its surface.

Figure 32. A sample of the same monolith as that of Figure 31 seen under a scanning electron microscope.

same monolith as that shown in Figure 31. It is interesting to note that the aerogel density used in Figure 31 is not the optimal density for absorption (5-20 mg/cc would have larger pore size and higher porosity), and yet we observed a propensity for both surface and bulk molecular sorption.

Figure 33 is a SEM micrograph (64.4x) of water deposited onto the surface of a sample of aerogel of density 349 mg/cc. It is remarkable that aerogel of this density, with much smaller pore size and pore density still collects and contains molecular contaminants, although microscopic survey showed this to be primarily a surface film. The highest density that a sol gel glass can be used for gettering action is 2.0 grams per cubic centimeter, or essentially full density glassey matricies still act as getters to varying degrees for certain species.
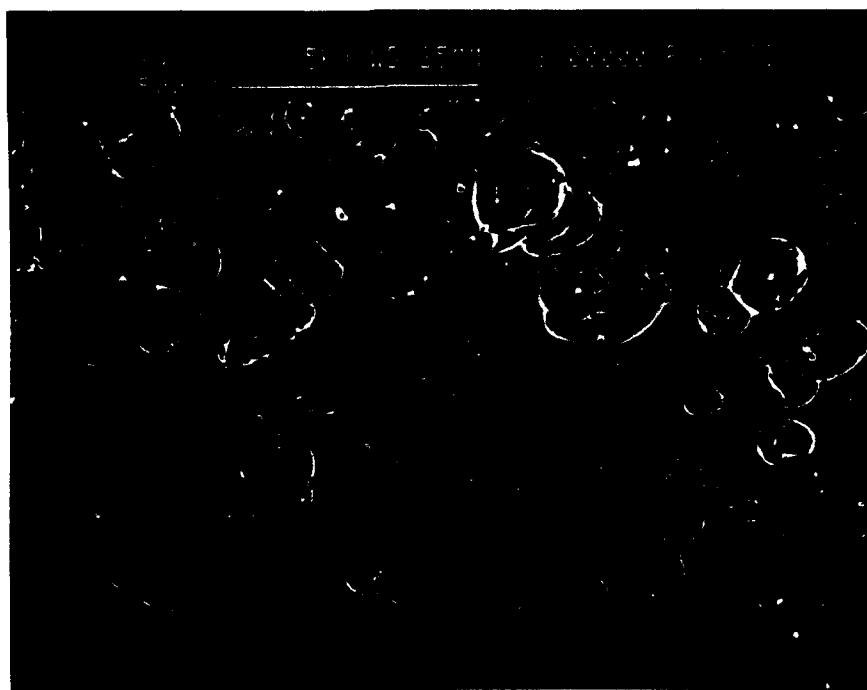

Figure 33. A SEM of a water film on the surface of 349 mg/cc aerogel.

Particulates were also collected by the aerogel as shown in Figures 34 and 35. Figure 34 shows an optical micrograph of graphite particles collected by a sample of aerogel of density 83 mg/cc. Microscopic survey showed various sized particles adhering to various strata in the aerogel structure; smaller particles penetrating deeper into the matrix. Figure 35 is a SEM micrograph of copper particles attached to the surface of a sample of aerogel of density 100 mg/cc. The copper particles were deposited onto the surface after being removed from a glass plate with a blast of compressed air. Subsequent mechanical agitation (by rapid acceleration of the SEM goinometer stage) failed to "shake loose" the observed copper particles, however it is clear that more quantitative experiments need to be persued, such as running a contaminated sample through the space shuttle launch vibration spectrum if the device is intended to be used in a shuttle application. As with the above samples, aerogel of this density is suboptimal for this application, yet the results are encouraging. Particulates may also be seen in the SEM micrograph Figure 36 although we do not know the type of this particulate contamination, or its origin.
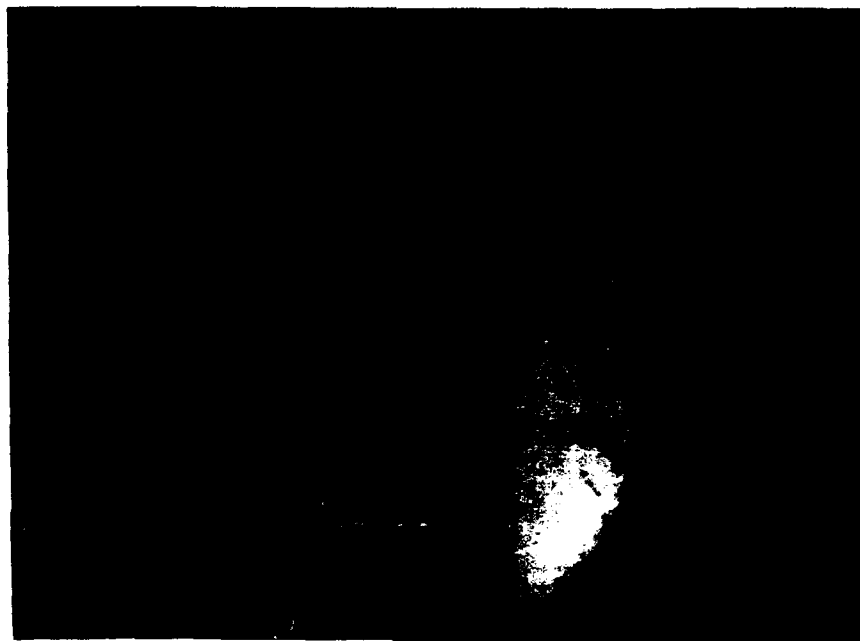

Figure 34. Particulates captured by aerogel pores.

Figure 35. A SEM of the AMCC with Cu and room dust particles attached.

6.0   Summary

This report presented the state of the theory and practice of the Aerogel Mesh Contamination Collector (AMCC) as studied under the Rome Laboratory project LDFP 12H2. The AMCC was found to be an improvement to the prior art getter technologies, so much so that two patent applications were filed for embodiments of the AMCC.

Prototype AMCC's were fabricated in this effort, but optimization was not performed. This fact notwithstanding, the preliminary results showed the AMCC to be operable over a wide temperature range : 4< T< 600 °K. The device was found to be remarkably radiation resistant (surviving up to 100 Mrads).

The engineering tests of the AMCC suggest that the AMCC should be studied in further detail for integrated circuit and photonic modules. The AMCC is applicable to several other technology areas such as biomedical and nuclear contamination control. The Aerogel Mesh Contamination Collector (AMCC) is a new *dual use* Air Force invention that can be designed into a variety of military and industrial systems. The dual use nature of the AMCC is delineated below.

(1) **Significance to the Military**: The Aerogel Mesh Contamination Collector (AMCC) may serve as a contamination collector for ground and air tactical and space-based infrared and visible optical systems—for which it is extremely capable: A contractor baselined the Aerogel Mesh Contamination Collector (AMCC) in a SDI space experiment and referred to it as *"...the only collector which can efficiently perform the mission..."*. Patents are pending on the Aerogel Mesh Contamination Collector (AMCC) for the following Air Force applications: satellite decontamination systems, integrated circuit

getters—conventional as well as millimeter wave integrated circuits (MMIC), microwave tube getters (*e.g.*, Klystrons), photonic integrated optical device package getters.

(2) **Technology Transfer—Defense Conversion Significance:** Patents are pending for the Aerogel Mesh Contamination Collector (AMCC) for use in the following systems: biomedical & particle separators, hospital operating room decontamination equipment, virus collectors, molecular sieves, nuclear waste collectors, gas filtration systems, and new semiconductor fabrication systems.

7.0 References

1. Proc. Mater. Res. Short Course on Polymers in Electronic and Phononic Integrated Circuits, 1991.

2. C.J. Brinker and G. Scherer, *SolGel Science*, Harcourt Brace and Jovanovich, (1990).

3. D.A. Dykeman and S.P. Hotaling, An Introduction to Rome Laboratory Contamination Control Tedhniques, RL-TM-92-18 (1992).

4. S.S. Kistler, J. Phys. Chem., 36, (1932)

5. A critical point dryer is a device usually used to dehydrate tissue for electron microscope examination. The technique was first establishedby Poloron Corporation in (1970). The device, previously known as the poloron, extracts HOH and/or OH and replaces it with liquid CO_2. Phase change from liquid CO_2 to vaporous CO_2 allows the selected sample to achieve dryness. Now BIO-RAD Microscience Division, BIO-RAD House, Maylands Avenue, Hemel Hempstead, Hertfordshire, HP2 &TD, England

6. S. Wagener, Proc. IEE, vol. 99, pt.3, (May 1952), 135-147.

7. S. Wagener, Vacuum, vol 3, no 1, (Jan. 1953), 11.

8. M. Knudsen, Annalen der Physik, 1901, 28, p999.

9. E.A. Flood, The Solid Gas Interface, vols I and II, Marcel Decker Press (1967).

10. B.G. Linsen, Physical And Chemical Aspects Of Adsorbents And Catalysts, Academic Press, (1970).

12. S.J. Gregg, Physical Adsorption of Gasses, in MTP International Rev. Sci., vol 7, Surface Chemistry And Colloids, M. Kerker (ed.), Butterworks Univ. Press (1972).

13. B.V. Derijaguin, Physical Absorption in The Solid Gas Interface, J.H. Schulman (ed), Academic Press (1957).

14. S. Bruunauer, SP.H. Emmett, E. Teller, Jou. Am. Ch. Soc.,60, (2),309, (1938).

15. R.K. Iler, The Chemistry Of Silica, J. Wiley & Sons, (1979).

16. R.H. Fowler, Proc. Cambridge Phil. Soc., 31, 260, (1935).

7.1 General References

7.1.1 Aerogels

1. S.P. Hotaling, Ultra-Low Density Aerogels for Advanced Optical Applications, RADC Office Memorandum (1990).

2. S.P. Hotaling, Ultra-Low Density Aerogel Optical Applications, Journal of Materials Research, Volume 8, Number 2, Feb. 1993, 352-355.

3. L. Hrubish, T. Tillotson, and F. Poch, *Better Ceramics Through Chemistry IV,* MRS PRESS (1990).

4. D.C. Bradley, et al., *Metal Alkoxides,* Academic Press (1978).

7.1.2 Contamination and Statistical Physics

1. S.P. Hotaling, Analysis of Leading Edge and Trailing Edge Samples from the LEDF Spacecraft Before and After Treatment with Advanced Contamination Control Techniques, Proc. High Power Optical Components Conf., ed. D.L. Decker (in Press).

2. S.P. Hotaling , D.A. Dykeman, An Advanced Particle and Molecular Contamination Identification, Removal and Collection System, (in the hard cover volume: *Particles On Surfaces IV,* ed, K.L. Mittal Plenum Press, (1993).

3. S.P. Hotaling, Adapting Military Technology For Civilian Use: Contamination Removal and Collection Techniques, MICROCONTAMINATION, May 1993, p 12 (in press).

4. S.P. Hotaling, An Advanced Contamination Control System, Proc. Microcontamination Conference, October 1992.

5. S.P. Hotaling and N.T. Castello, Microcontamination: Detection, Identification, Removal, and Collection System, Proc. Government Microcircuit Applications Conference, (1992).

6. S.P. Hotaling, Proc. LDEF Materials Results for Spacecraft Applications Conf., Huntsville AL, 1992.

7. S.P. Hotaling , Proc. Space Technology Interdependency Group Meeting, Nov. 1992.

8. S.P. Hotaling, D.A. Dykeman, An Introduction To Rome Laboratory Contamination Control Technology, RL-TM-92-18 (1992).

9. S.P. Hotaling, The Aerogel Mesh Contamination Collector, Rome Laboratory Final Report for RL-LDFP 12H2, (in press).

10. L.D. Landau and E.M. Lifshitz, Statistical Physics, Part I, Pergammon Press (1980).

Appendix A   CONTAMINATION REMOVAL AND COLLECTION

A.1 Introduction

Contamination can be either particulate or molecular in nature. There are many sources of these species which can vary throughout the lifetime of a component or system. The contamination impact is just as varied, depending on atmospheric conditions, contaminant and component charateristics, deposition mechanism, rate and aging, etc. New data presented by the autohor at the 1992 High Power Optical Components Conference, suggests that for external spacecraft surfaces, whether in the RAM or not, that the synergistic effects of contamination, radiation and space plasmas create a new class of problems for on orbit maintenance [3].

A.2 Particulate Contamination

Particulate contamination arises from a multitude of sources. Even ultra-clean environments such as semiconductor processing facilities utilizing high efficiency particle absolute (HEPA) filters are not devoid of particles in the air and on exposed surfaces. In such environments, personnel, frictional contact between tools and product, robotic device movements and equipment vibration create particles. Also, air currents act to redistribute the particles. Particles can be either organic or inorganic in nature. Inorganic particles tend to be harder and more spherical in geometry than organics. They typically range in size from less than 1 micron (Ref. Figure A1) to hundreds of microns in diameter (Ref. Figure A3). Particles are generated by friction between surfaces, surface erosion due to atmospheric chemical interactions or other process related operations including PECVD. Figure A1 is a field emission SEM (FESEM) photomicrograph showing several submicron sized particles

on a silicon substrate. These particles although small, resulted in device failure. Figure A2 illustrates incomplete metalization (Al on Si) due to the presence of the submicron particle shown in the center of the figure. Figure A3 illustrates a large silica particle on a silicon wafer which originated during a silane PECVD deposition process. Presumably the particle was formed on the walls of the PECVD chamber and thence fell onto the wafer surface.

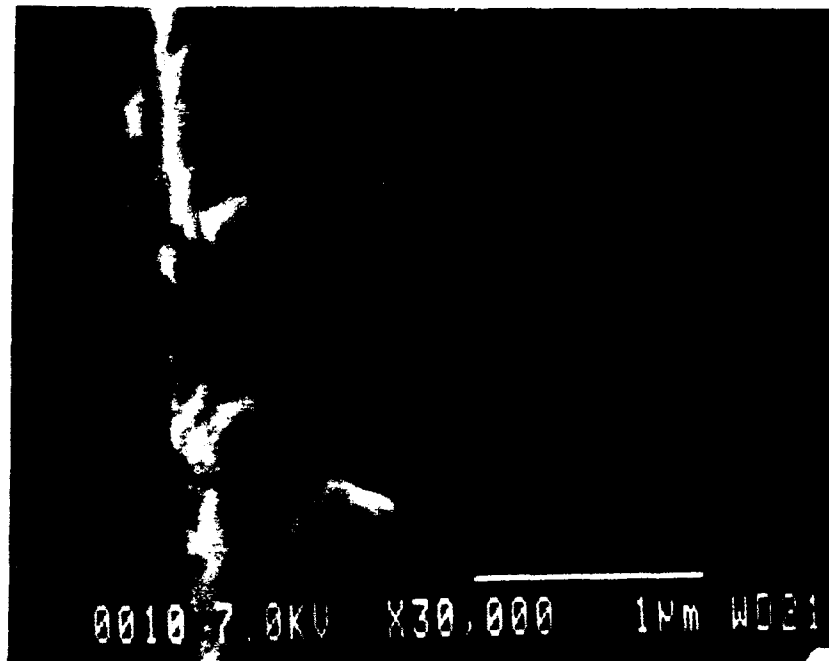Figure A1. Submicron particulates on Silicon.

Figure A2. Micrometer sized contaminates which caused incomplete metalization on a GaAs solid state laser.
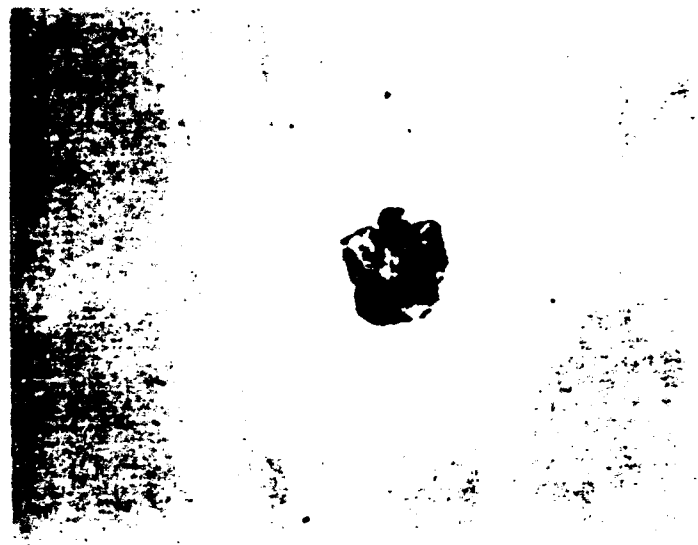

Figure A3. A silica particle found on a wafer after a PECVD process. The silane decomposition process caused a silica particle to form on the wall and subsequent mechanical vibration caused it to come to rest on the substrate.

71

The FESEM is useful for the **detection** of submicron particles on dielectric

substrates; a situation which usually leads to charging and thus poor resolution. For

production line inspection, FESEM is not practical leading to the use of optical microscopy

such as Dark Field, Nomarski, and Fluorescence techniques as illustrated in Figure A4.

Figure A4a is a Nomarski optical photomicrograph of a sample taken from the LDEF

(Long Duration Exposure Facility: Figure A4d) which has been selectively subjected to the

reactive oxygen ion beam cleaning technique (brown featureless area) and masked with a

glass cover slide illustrating the effect of the ion beam contamination removal. (The ion

beam cleaner will be discussed later in the article). To the eye, the sample appears to have

A4a
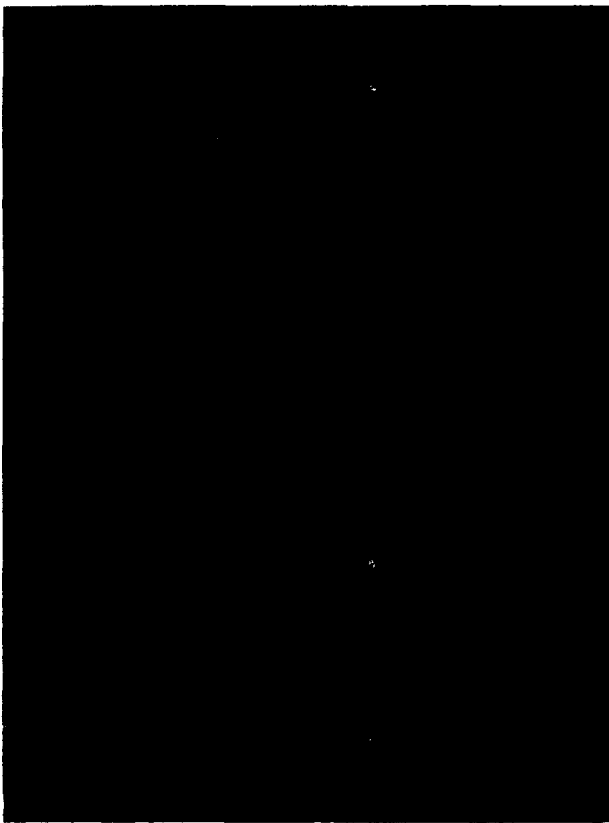
A4b

Figure A4. Nomarski (left) and Dark Field Micrographs of LDEF leading
edge sample before(lower left) and after (upper right) ion beam cleaning.

A4c

A4d

Figure A4. c: Fluorescence Light Micrograph of sample before (left) and after cleaning (right) with ion beam cleaner. d: LDEF on orbit.

no physical defects, however upon Dark Field microscopic inspection, shown in figure 4b, the presence of surface defects becomes apparent. The particulate contaminant defects were removed by the CO_2 Gas Solid Jet Spray technique (to be discussed later in the article). The detection of thin molecular films (thicknesses < approx. 30 angstroms) is sometimes difficult using Nomarski microscopy because this film thickness is very close to the limit of detection for Nomarski Microscopy. In this case, a florescence light micrograph may be revealing as shown in Figure A4c. Here, an organic film detected by Nomarski fluoresces brightly. The detection of submicron contamination may also be aided by use of real time computer image analysis as shown in Figure A5. Here we make use of the *MacPhase* computer analysis software to enhance faint shadows of a dendritic film (bright colors against a forest green background in image space and by computing weighted Fourier Transforms of the digitized image, compare the frequency content of the contaminated surface before cleaning (Figure A5b) to that after cleaning (Figure A5c). The author has also learned of the existence of a computer system which performs similar analysis on the SEM using an advanced workstation.

Once detected, the contaminant must be **identified** so as to determine its origin and points of entry into the production line. The combination of FT-IR (Fourier Transform Infrared), EDX (Energy Dispersive x-ray), AES (Auger Electron), and XPS (x-ray Photo emission) Spectroscopies have been successful for us in this task. For submicron dielectric particles on a semi-insulating substrate however, the EDX signature from the FESEM is of particular utility as illustrated in Figure A6. In the figure, the difference between a silica substrate and micron-sized Pb particles is illustrated. Using a conventional SEM, this type of data is difficult to obtain due to substrate and contaminant charging. In addition to these detection and identification techniques, it may be of interest to investigate surface enhanced Raman techniques.

A 3. Molecular Contamination

Molecular contaminants result from a variety of processes including outgassing of polymeric or organic materials, residual molecules from chemicals used in component processing, desorption and/or diffusion, and condensation and absorption from the

contam.fftmag.den   dend.cln.fft.mag
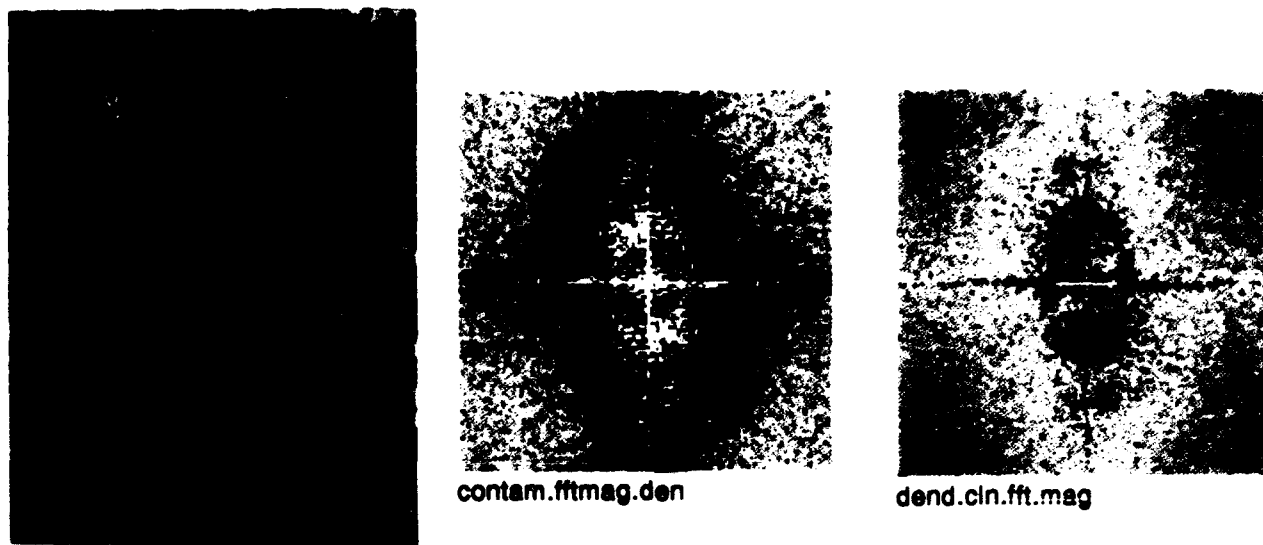
FigureA5. MACPHASE enhanced image of a section of the LDEF leading edge
sample which showed dendritic growth. Figures 5b and 5c are the magnitude
plots of the FFT computed over the contaminant area of Figure A5a (b) versus
the same over the cleaned area (c). Macphase's false color and digital filter
algorithims provide enhanced image analysis capability. Note that the FFT of
the contaminated section has large magnitude low frequency plus the high
frequency components, whilst the FFT of the cleaned section has much lower
low frequency contribution. Thus the FFT can be used as a measure for
contamination on surfaces.

environment. Condensed matter contains sorbed gases which diffuse and desorb from free

surfaces envacco - especially at elevated temperatures (such as found in semiconductor

CVD chambers and spacecraft). The largest source of outgassing in these applications
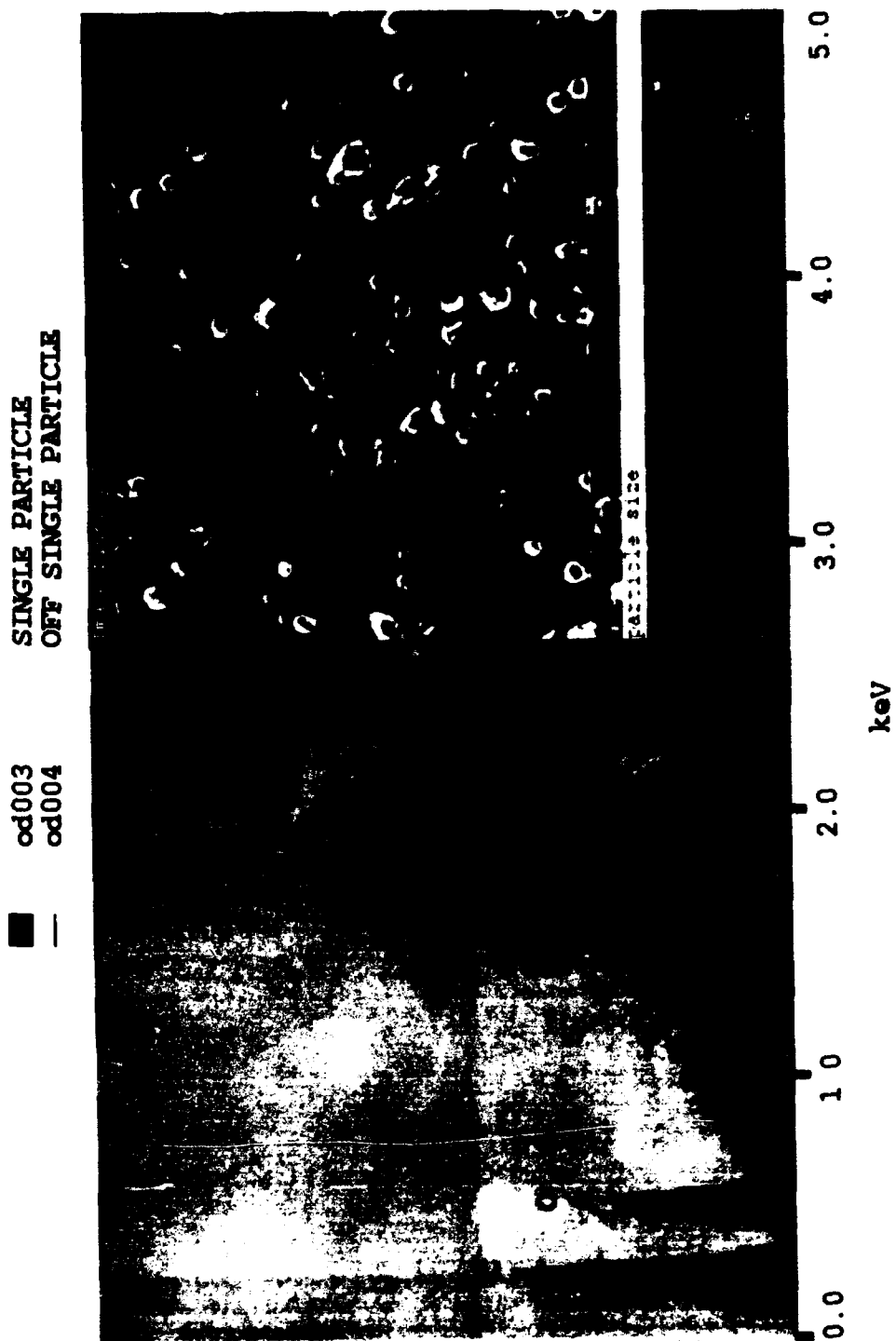
Figure A6. Energy Dispersive X-ray measurement of particles shown in upper right of figure.

originates from insulating and process materials such as polymers. Polymers are not only complex molecular species (by definition), but also may contain undesired systhesis and or process residual species (incompletely polymerized base monomers or molecular species left over from polymer manufacturing, forming or additives such as nucleating agents, stabilizers, plasticizers, etc.) which may desorb along with the atmospherically sorbed gases. Thermal energy imparted to substrates during processing may further decompose polymers into volatile compounds which (of course) are potential contaminants.

Outgassing is a complex physical phenomenon in which molecular species are released by a material by a variety of processes including diffusion, surface desorption or catalysis. The outgassed species are then free to come to rest or condense onto surfaces within a few mean free paths Condensation is essentially a deposition process involving nucleation, island growth, surface diffusion, and monolayer buildup. The physical and chemical kinetics of multi-component species deposition onto a surface could give rise to a potpourri of amorphous and polycrystalline molecular films. Both the outgassing and the deposition processes are temperature and time dependent.

Diffusion: Consider the condensed matter system comprised of an intrinsic substrate with contaminant species offgasing to be modeled as an embedding in a three dimensional Euclidean manifold with the offgassing species having a concentration given by the field C. The one-dimensional flow rate may be generally expressed by Fick's laws (Cf. 1850). Fick's first law is :

$$F = -D \frac{\partial}{\partial x} C.$$
(A1)

Where in $\mathbb{E}^{(3)}$, F is the flow rate per unit area and C is the local concentration field of the offgassing material. Since the volume three-form in $\mathbb{E}^{(3)}$ is

$$\tilde{\omega} = \tilde{d}x^1 \wedge \tilde{d}x^2 \wedge \tilde{d}x^3$$
(A2)

assuming the manifold is endowed with a connection, then from compatibility, the Fick law for a spatially and temporally varying C-field, we obtain:

$$\partial_t C = \mathfrak{t}_{\tilde{c}} (D \vee C \tilde{\omega})$$
(A3)

Where: $\mathcal{L}_{\vec{c}}$ is the Lie derivative giving the divergence in the manifold[6]. This assumes the rate

to be proportional to the concentration gradient. The diffusion "constant" D, is given by:

$$D = D_0 e^{(1-E_d/KT)} \tag{A4}$$

is the diffusion equation with E_d expressing the diffusive activation energy in the system.

Desorption: Once the diffusing species reach a free surface, they become part of

the gas/solid interface and have a desorption probability. The statistical thermodynamics of

the exchange between adsorbed and desorbed states is treated via the Langmuir and BET

theories which are discussed in the next section. Even in a system in which all components

have been vacuum baked, this process is possible. It is partly in response to this problem

that the **AMCC** (Aerogel Mesh Contamination Collector) was invented. The AMCC

concept is to present offgassed contaminants with an energetically more favorable surface to

adsorb onto rather than the critical substrate (satellite optic, semiconductor wafer, or other

substrate of interest). The adsorption of molecular films will cause the surface's sticking

coefficient to increase, attracting and holding contaminants and acting as nucleating sites for

further molecular deposition. Thus, the rate of contamination increases with time. Exposure

to ultraviolet radiation can cause photo-induced catalysis of organic molecules. This is

especially of concern in the outgassing of plasticizers from vinyl curtains or floor tiles as

well as from process chemicals[4] in clean rooms. Polymerized organics become "fixed" to

surfaces and are extremely hard to remove. Even the low intensities of short wave ultraviolet

radiation (1800 angstrom wavelength) leakage from fluorescent lighting may be a cause of

photoinduced conversion of organic vapors into particles[7,8,9]. The source of organic vapors

in clean rooms is presently suspected to be due to outgassing of organic vapors from vinyl

curtains or floor tiles as well as from process chemicals[8]. The most effective method of

organic removal (used by the author to date) is low energy reactive oxygen ion etching. The

oxygen ions chemically react with the organic to break it down into volatile species. It is

also possible to utilize the combination of supercritical CO_2 and ultrasonic energy to

remove molecular films[10] (the author is in preliminary stages of this experimentation at present-the first samples have been run but results as yet are inconclusive).

A 4. Jet Spray Contamination Removal

The system designed and used by the author is shown in Figure A7. The system (built in-house) is essentially only a slight modification to the Hoenig system;of which there are many variants used in industry today. The choice of materials is of importance in the system; the use of inferior materials has been shown to actually produce submicron sized particles. Figure A7 contains a cartoon illustrating the jet spray operation. The cleaning mechanism is momentum transfer. A stream comprised of solid particles within a gas is incident upon a contaminated surface. The particles are dislodged from the surface by momentum transfer from the solid "snowflakes" and both are then carried away from the surface by the gas. The jet spray has been very effective in removing particles from room temperature optics and semiconductors and both particles and thin cryofilms have been removed from cryogenic optics[11].

This system has been used by the author for room temperature cleaning of silicon wafers, glass, germanium wafers, and complex piece parts. Glass chips (formed by a diamond glass cutter) adhering to water vapor rich glass microscope slides which were left to dry at room temperature for hours were also removed using this system. Such particles (hundreds of microns in diameter) are known to be very difficult to remove due to very high surface forces between two flat surfaces (a dried water film notwithstanding). To demonstrate this, one only need perform the following simple exercise: *Prepare two identical microscope slides as follows: superglue flat head bolts to the "dirty" sides of the slides. When cured, allow a water vapor film to populate the clean side of one of the slides. Press the clean surface of the other slide against the moist slide. Place the system in a tensile testing apparatus and note that it takes several hundred psi to disjoin the slides. In*
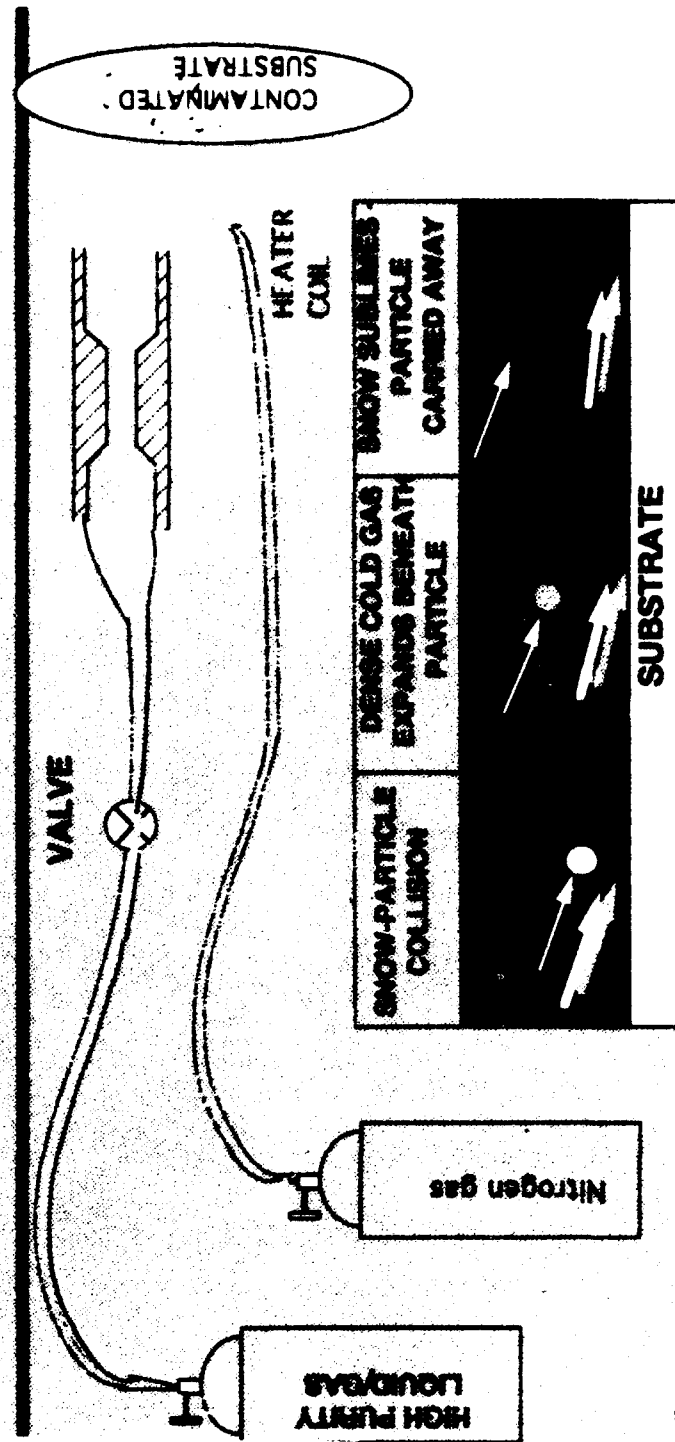
Figure A7. A schematic of the RL In-House Jet Spray designed and built by the author.

fact, although less sheer force is required, to achieve separation, the acutal magnitudes of
these surface forces illustrate the point very effectively. Although qualitative in nature, this is
a major piece of applications data for the high tech. glass working community concerned
with removal of process induced micron to hundreds of microns sized glass chips from
scoring and cleaving operations.

Figure A8 illustrates the results of cleaning a sample from a high velocity particulate
"dirt gun" contaminaton process. Figure A8a is a 35mm before-cleaning photograph of the
sample and Figure A8b is the sample after cleaning. The sample was a high tech. optical
substrate. It is possible that the jet spray cleaning technique may be applied to critical
process equipment (e.g. wafer holders and vacuum chucks), semiconductor wafers, finished
chips prior to and following encapsulation, and complex parts such as ring laser gyro
frames. *In addition to high cleaning efficiency, this technique can potentially obviate the use*
of CFC's in accordance with new environmental regulations. Additionally, it is feasible
that the Jet Spray could be used to decontaminate radioactive samples(eg. samples from
underground nuclear tests) without creating radioactive liquid waste products.

It has been suggested that there is some possibility of the solid CO_2 particles
scratching or otherwise degrading the substrate. This is an understandable concern, but the
author has not found evidence of this in his work. Indeed, if large, high momentum CO_2 ice
pellets are allowed to strike the substrate rather than an even flow of controlled momentum
snowflakes in a heated gas mixture, it is possible to damage the substrate. A possible model
for the CO_2/substrate interaction was performed by Hoenig at the University of Arizona (cf.
1985). He suggests that it is possible that the process is Lidenfrost-like in nature. As such,
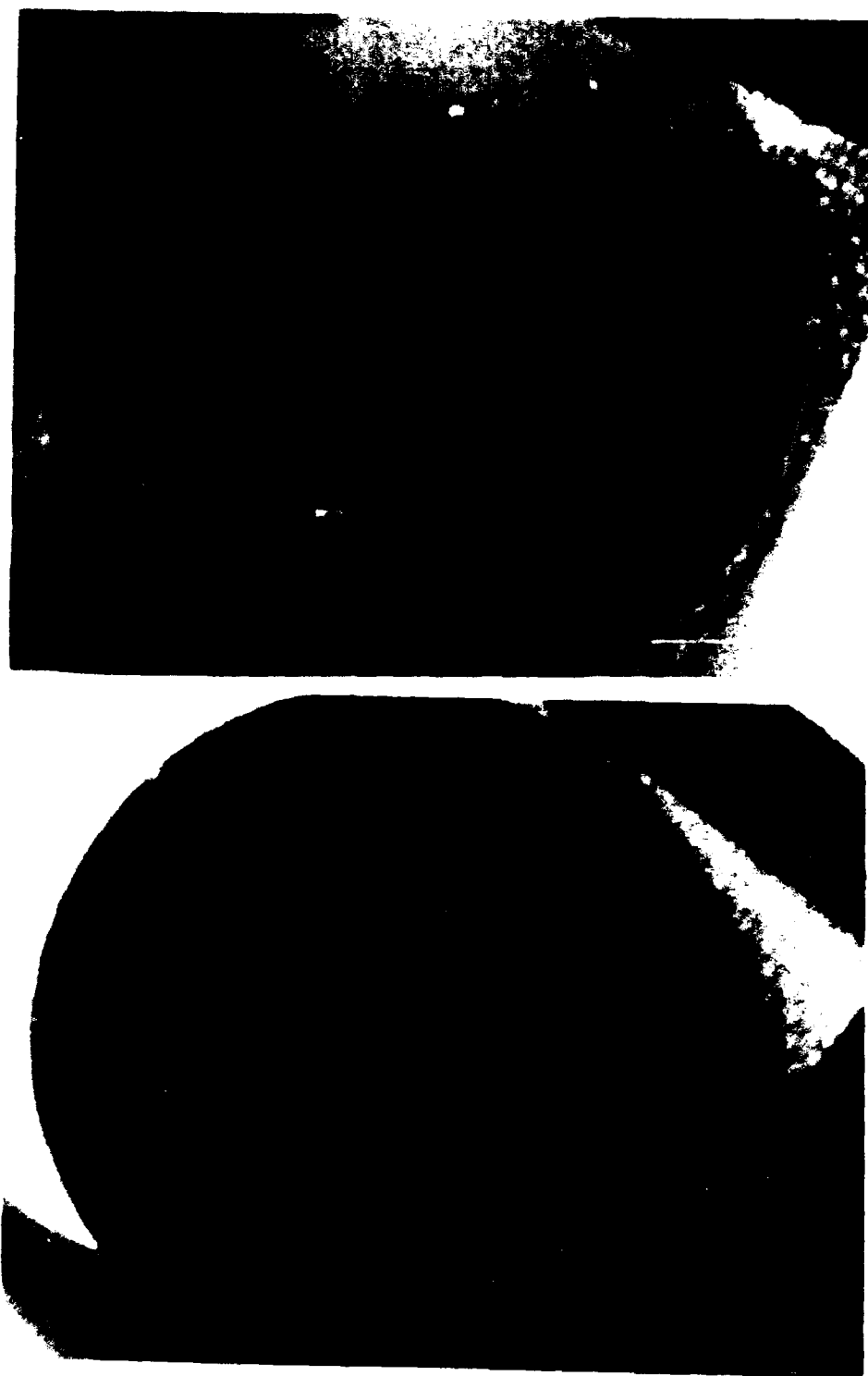his model follows a thermodynamic approach starting with the radiation input to the

Figure A8. Jetspray demonstration. Top mirror is covered with large dirt particles which were deposited at high velocity. The bottom photo is same mirror after treatment with jet spray.

snowflake Q:

$$Q = \frac{\sigma \pi D^2}{4}\left(T_s^4 - T_f^4\right) \tag{A5}$$

Where D is the diameter of the snowflake, and σ is the Steffan Boltzman constant. The s-subscript refers to the substrate and the f refers to the snowflake. If m is the rate of evaporation and H_v is the heat of vaporazation, then Q may be written:

$$Q = H_v m \tag{A6}$$

or, that the rate of evolution V is given by:

$$V = m / \rho \tag{A7}$$

Where ρ is the density of the CO_2 gas. Thus,

$$V = \frac{m}{\rho} = \frac{Q}{H_v \rho} \tag{A8}$$

If h is the height of the CO_2 snowflake above the surface and U its velocity, then the volume swept out at that U is:

$$v = UDh \tag{A9}$$

and substitution into equations 5-8 gives:

$$V = \frac{m}{\rho} = \frac{Q}{H_v \rho} = \frac{\sigma \pi D^2}{4h\rho}\left(T_s^4 - T_f^4\right) \tag{A10}$$

Using typical values the height above the surface is in the range: $0.1 < h < 1.0$ (micron). This implies that if the Lidenfrost-like model for the process is correct, then the average CO_2 snow particle does not touch the surface and hence there is little probability of CO_2 snow-induced surface degradation.

It has also been found that trace amounts of small metal flakes or pump oil have been identified on surfaces treated with CO_2 snow. These problems are avoided by using ultra-high purity CO_2, high quality metal filters in the CO_2 transfer line and a jet spray

nozzle fabricated from high quality materials which do not degrade upon interaction with prolonged use.

To visualize the Jet Spray process, the author focused an optical microscope on a glass substrate which was sparsely contaminated with room fallout. The microscope was instrumented with a CCD video camera, VCR and computer interface. The Jet Spray was photographed in operation at several flow and temperature settings determining snowflake size and momentum as well as substrate temperature. The VCR recording was selectively sampled frame by frame with the data bearing frames being digitized and stored for MacPhase computer image analysis. Figure A9a is a frame of the VCR tape at a magnification of 10x which has been digitized and *MacPhase* enhanced to show the CO_2 snowflake size and density distribution (as focused on the glass substrate). Figure A9b illustrates another frozen/digitized VCR video frame at a magnification of 450x. The dark spots are the CO_2 snowflakes. Other results of this experiment captured on the VCR tape illustrate the effects of insufficient heated Nitrogen gas flow combined with very high CO_2 flow rate leading to the formation of ice on the glass substrate surface

Figure A9a.   The jet spray in operation.   Freeze frame photos of the RL jet spray viewed under a microscope interfaced to a VCR and frame grabber.   Macphase was used to enhance the image.   This allows snowflake statistical data to be generated
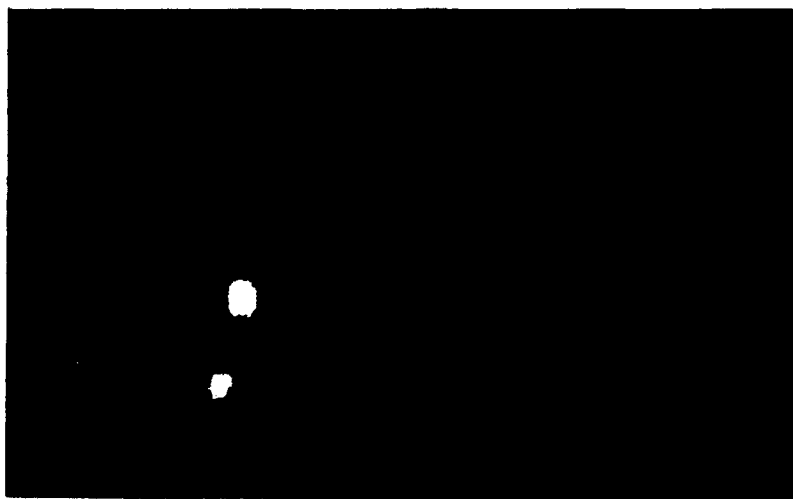
Figure A9b. High magnification, digitally enhanced Freeze Frame CO_2 snowflake imaged with Macphase.

A5. Electron/Ion Contamination Removal

Electron contamination removal can either be done through electronic heating of the substrate with subsequent contaminant vaporization or by electronic sputtering. The more efficient, i.e. quicker with less potential for substrate damage, method is electronic sputtering which is depicted in Figure A10. The incident electron's kinetic energy is transferred to the contaminant atom via the atom's electron cloud as opposed to direct ion to contaminant atom momentum transfer as in ion sputtering. *Low energy* oxygen ions (less than 10 eV) will remove organic contaminants without damage to the substrate. The oxygen ion reactive etching process is illustrated in Figure A12 and a laboratory model of the Hughes Helicon Wave Source (ion beam source) used in this work appears in Figure A12. The oxygen ions chemically react with the film to break it down into volatile species which are then easily removed. The chemical mechanism allows for low energy ions to be used thus reducing the chance of substrate damage.
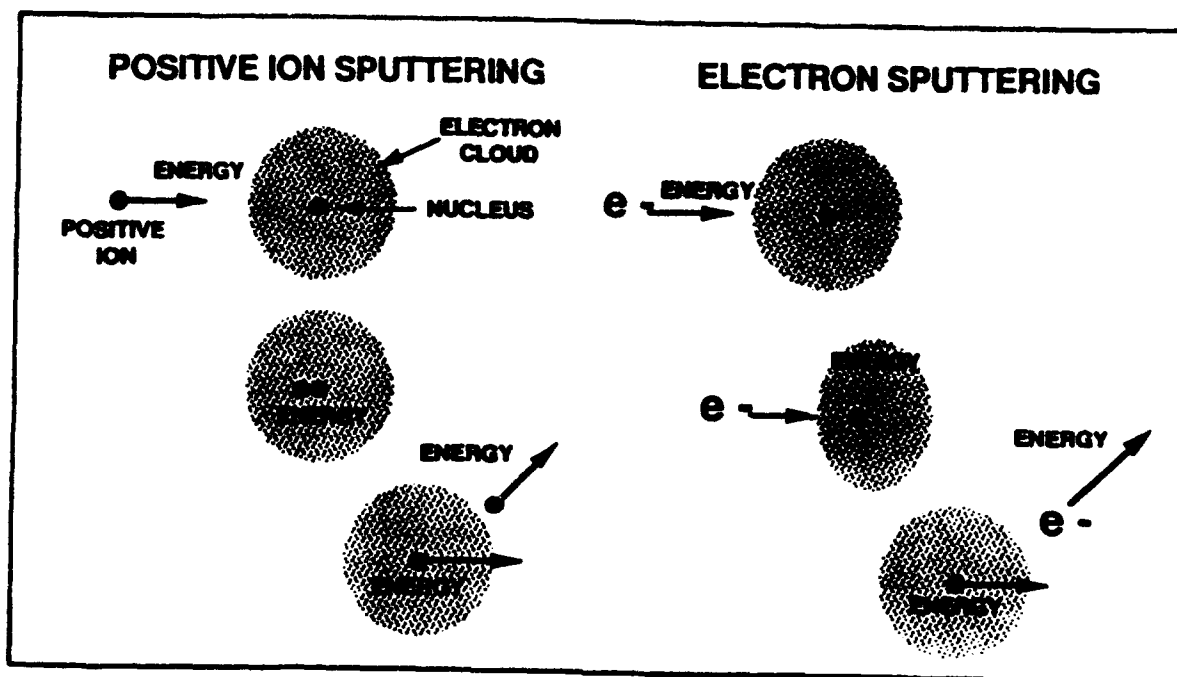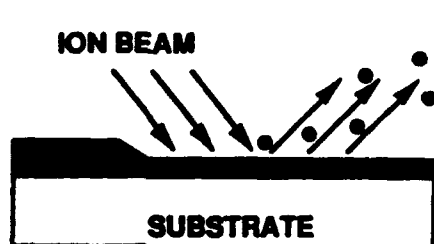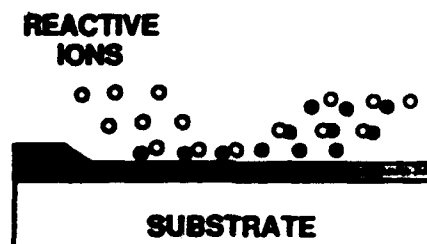
POSITIVE ION SPUTTERING

ELECTRON SPUTTERING

Figure A10 Ion vs. Electron sputtering cleaning processes illustrated. Ion sputtering utilizes direct transfer of kinetic energy from the incoming ion to the contaminant atom nucleus. Electron sputtering involves the energy transfer between incoming electrons and the contaminant atom's electron cloud.

KINETIC ENERGY TRANSFER FROM INCIDENT ION TO CONTAMINANT

ION REACTS CHEMICALLY WITH CONTAMINANT SPECIES. CHEMICAL ENERGY IS CONVERTED TO KINETIC ENERGY. RESULTING MOLECULES ARE VOLATIZED.

SPUTTER YIELD = f(ION ENERGY)
REMOVAL TIME = f(ION CURRENT DENSITY)
IONIZATION EFFICIENCY = f(ION TYPE)

Figure A11 Direct Ion Etch and Reactive Ion Etch cleaning processes illustrated.

86

The results of cleaning organic molecular films and particulates is illustrated in

Figure A12a-A12c. Here the gas/solid jet spray and ion beam contamination removal
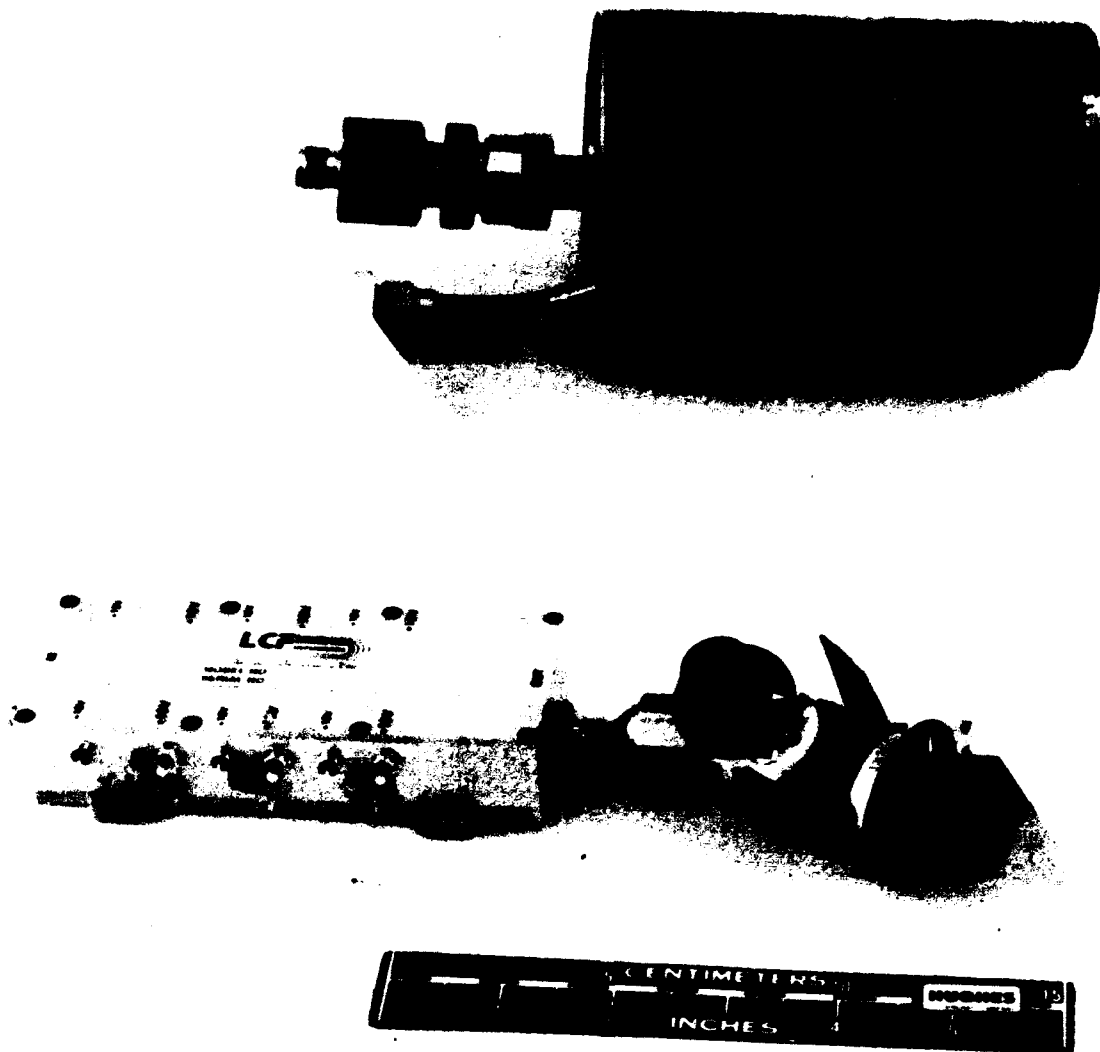

Figure A12. The Hughes HWS Ion Beam Source (seen here in split view).

techniques were applied to a silicon wafer which flew in low earth orbit (LEO) on the LDEF satellite for 69 months. This sample is far more contaminated than any used in IC fabrication, and hence serves as a worst case example of contamination. The performance obtained by these contamination control techniques is a very compelling argument for the efficacy of these techniques. The sample was contaminated with an organic molecular film 5000 angstroms in thickness which was photo-polymerized due to exposure to UV radiation of the LEO environment. Auger, EDX, ESCA and FT-IR spectroscopies were used to identify the contaminants. These Spectroscopies indicate that the particles were both organic and metallic in nature (aliphatic hydrocarbons, metals and siloxanes), and are most likely contaminant species from the spacecraft. Figure A13a shows a cross polarized light micrograph of a section of the LDEF crystalline Si sample as received. The results of 30 minutes of treatment with reactive oxygen cleaning appear in Figure A13b. Note that most of the film has been removed. It is suspected that for most laboratory generated organics, much less than 15 minutes would be required for removal. Figure A13c shows the sample after 1 hour of treatment with the ion beam technique. Surface spectroscopic identification techniques failed to show the presence of contaminants after this treatment.
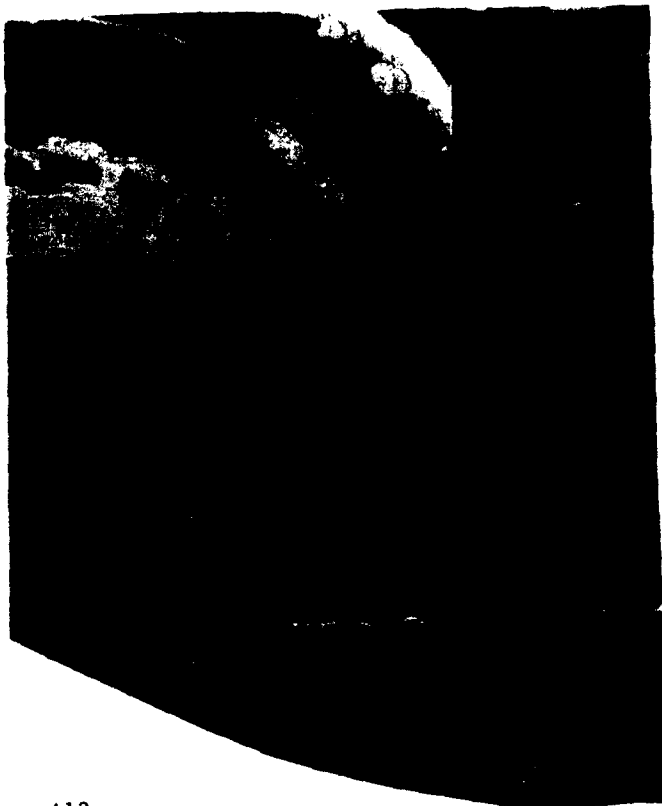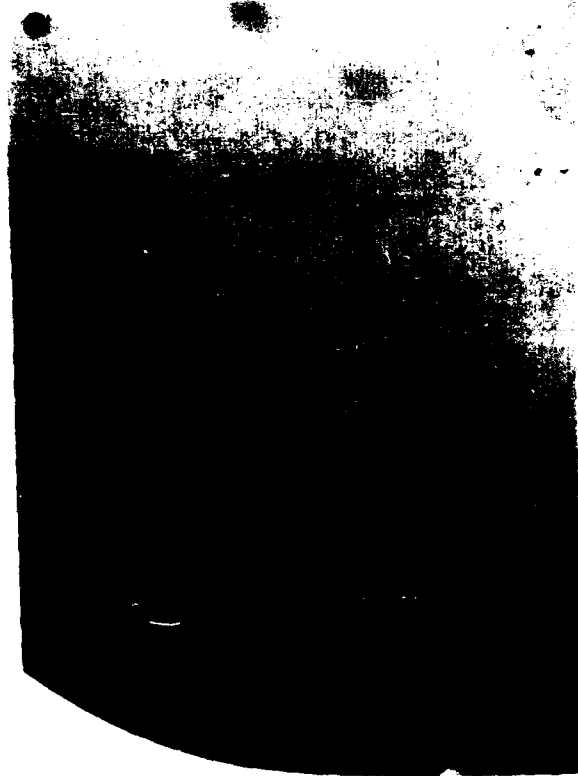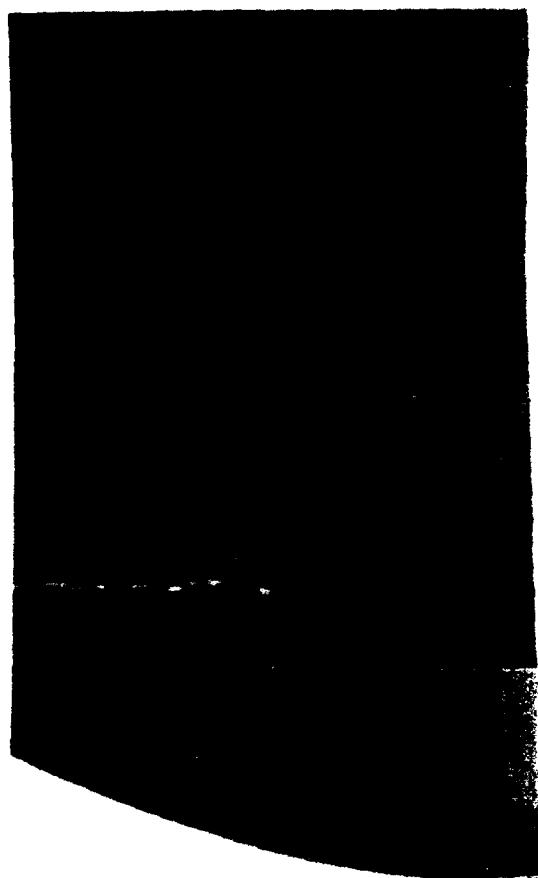
A13a   A13b

Figure A13. Cross polarized light micrographs of LDEF leading edge samples in three states of cleaning. A13a: as received. A13b. Sample condition after 30 minutes cleaning. A13c (next page): The state of the sample after 1 hour ion treatment.

A13c.   Same Sample as Figure A13 a after 1 hour ion beam treatment.

MISSION

OF

ROME LABORATORY

Rome Laboratory plans and executes an interdisciplinary program in research, development, test, and technology transition in support of Air Force Command, Control, Communications and Intelligence (C3I) activities for all Air Force platforms. It also executes selected acquisition programs in several areas of expertise. Technical and engineering support within areas of competence is provided to ESC Program Offices (POs) and other ESC elements to perform effective acquisition of C3I systems. In addition, Rome Laboratory's technology supports other AFMC Product Divisions, the Air Force user community, and other DOD and non-DOD agencies. Rome Laboratory maintains technical competence and research programs in areas including, but not limited to, communications, command and control, battle management, intelligence information processing, computational sciences and software producibility, wide area surveillance/sensors, signal processing, solid state sciences, photonics, electromagnetic technology, superconductivity, and electronic reliability/maintainability and testability.